PHYSICAL REVIEW B **83**, 054407 (2011)

Statics and dynamics of weakly coupled antiferromagnetic spin-$\frac{1}{2}$ ladders in a magnetic field

Pierre Bouillot,[1] Corinna Kollath,[2] Andreas M. Läuchli,[3] Mikhail Zvonarev,[4,5] Benedikt Thielemann,[6] Christian Rüegg,[7]
Edmond Orignac,[8] Roberta Citro,[9] Martin Klanjšek,[10,11] Claude Berthier,[11] Mladen Horvatić,[11] and Thierry Giamarchi[1]
[1]*DPMC-MaNEP, University of Geneva, CH-1211 Geneva, Switzerland*
[2]*Centre de Physique Théorique, Ecole Polytechnique, CNRS, F-91128 Palaiseau Cedex, France and*
Département de Physique Théorique, University of Geneva, CH-1211 Geneva, Switzerland
[3]*Max Planck Institut für Physik Komplexer Systeme, D-01187 Dresden, Germany*
[4]*Department of Physics, Harvard University, Cambridge, Massachusetts 02138, USA*
[5]*Laboratoire de Physique Théorique et Modèles Statistiques (LPTMS), CNRS and Universite Paris-Sud, UMR 8626,*
Bâtiment 100, F-91405 Orsay, France
[6]*Laboratory for Neutron Scattering, ETH Zurich and Paul Scherrer Institute, CH-5232 Villigen, Switzerland*
[7]*London Centre for Nanotechnology and Department of Physics and Astronomy, University College London,*
London WC1E 6BT, United Kingdom
[8]*Laboratoire de Physique de l'École Normale Supérieure de Lyon, UMR 5672, CNRS, F-69364 Lyon Cedex 07, France*
[9]*Dipartimento di Fisica "E. R. Caianiello" and Institute CNR-SPIN, Universitá degli Studi di Salerno, Via Ponte don Melillo,*
Fisciano, I-84084 Salerno, Italy
[10]*Jožef Stefan Institute, Jamova 39, 1000 Ljubljana, Slovenia*
[11]*Laboratoire National des Champs Magnétiques Intenses, CNRS (UPR 3228) Université J. Fourier Grenoble I,*
Université de Toulouse, UPS, Institut National des Sciences Appliquées (INSA), F-38042 Grenoble Cedex 09, France
(Received 7 September 2010; published 9 February 2011)

We investigate weakly coupled spin-1/2 ladders in a magnetic field. The work is motivated by recent experiments on the compound $(C_5H_{12}N)_2CuBr_4$ (BPCB). We use a combination of numerical and analytical methods, in particular, the density-matrix renormalization group (DMRG) technique, to explore the phase diagram and the excitation spectra of such a system. We give detailed results on the temperature dependence of the magnetization and the specific heat, and the magnetic-field dependence of the nuclear-magnetic-resonance relaxation rate of single ladders. For coupled ladders, treating the weak interladder coupling within a mean-field or quantum Monte Carlo approach, we compute the transition temperature of triplet condensation and its corresponding antiferromagnetic order parameter. Existing experimental measurements are discussed and compared to our theoretical results. Furthermore, we compute, using time-dependent DMRG, the dynamical correlations of a single spin ladder. Our results allow to describe directly the inelastic neutron scattering cross section up to high energies. We focus on the evolution of the spectra with the magnetic field and compare their behavior for different couplings. The characteristic features of the spectra are interpreted using different analytical approaches such as the mapping onto a spin chain, a Luttinger liquid or onto a *t*-*J* model. For values of parameters for which such measurements exist, we compare our results to inelastic neutron scattering experiments on the compound BPCB and find excellent agreement. We make additional predictions for the high-energy part of the spectrum that are potentially testable in future experiments.

DOI: 10.1103/PhysRevB.83.054407 PACS number(s): 75.10.Jm, 75.40.Gb, 75.40.Cx, 75.30.Kz

I. INTRODUCTION

Many fascinating magnetic properties of solids are related to quantum effects.[1] In particular, due to the Pauli principle, the interplay between interactions and kinetic energy can induce a strong antiferromagnetic spin exchange. Such exchange leads to a remarkable dynamics for the spin degrees of freedom. On simple structures, the antiferromagnetic exchange can stabilize an antiferromagnetic order. By variations in dimensionality and connectivity of the lattice a variety of complex phenomena can arise.

Recently, among those effects two fascinating situations in which the interaction strongly favors the formation of dimers have been explored in detail. The first situation concerns a high-dimensional system in which the antiferromagnetic coupling can lead to a spin liquid state made of singlets along the dimers. In such a spin liquid the application of a magnetic field leads to the creation of triplons that are spin-1 excitations. The triplons that behave essentially as itinerant bosons can condense, leading to a quantum phase transition that is in the universality class of Bose-Einstein condensation[2–4] (BEC). Such transitions have been explored experimentally and theoretically in a large variety of materials, belonging to different structures and dimensionalities.[5] On the other hand, low-dimensional systems behave quite differently. Quantum fluctuations are extreme, and no ordered state is usually possible. In many quasi-one-dimensional (1D) systems, the ground-state properties are described by Luttinger liquid (LL) physics[6,7] that predicts a *quasi*-long-range order. The elementary excitations are spin-1/2 excitations (spinons). They behave essentially as interacting spinless fermions. This typical behavior can be observed in spin ladder systems in the presence of a magnetic field. Although such systems have been studied theoretically intensively for many years in both zero[8–16] and finite magnetic field,[2,17–27] a *quantitive* description of the LL low-energy physics remained to be performed specially for a direct comparison with experiments.

Quite recently, the remarkable ladder compound[28] $(C_5H_{12}N)_2CuBr_4$, usually called BPCB [also known as

$(\mathrm{Hpip})_2\mathrm{CuBr}_4$], has been investigated. The compound BPCB has been identified to be a very good realization of weakly coupled spin ladders. The fact that the interladder coupling is much smaller than the intraladder coupling leads to a clear separation of energy scales. Due to this separation, the compound offers the exciting possibility to study both the phase with LL properties typical for low-dimensional systems *and* the BEC condensed phase typical for high dimensions. Additionally, the magnetic field required for the realization of different phases lies for this compound in the experimentally reachable range. The LL predictions have been quantitatively tested for magnetization and specific heat,[29] nuclear magnetic resonance[30] (NMR), and neutron-diffraction (ND)[31] measurements. Additionally, the BEC transition and its corresponding order parameter have been observed experimentally by NMR[30] and ND measurements.[31]

In addition, the excitations of this compound have recently been observed by inelastic neutron scattering (INS)[32,33] experiments. These are directly related to the dynamical correlations of spin ladders in a magnetic field. These dynamical correlations hardly have been investigated so far. The direct investigation of such excitations is of high interest, because they not only characterize well the spin system, but the properties of the triplon and spinon excitations are also closely related to the properties of some itinerant bosonic and fermionic systems. Indeed, by using such mappings[6] of spin systems to itinerant fermionic or bosonic systems, the quantum spin systems can be used as quantum simulators to address some of the issues of itinerant quantum systems. One of their advantages, compared to regular itinerant systems, is the fact that the Hamiltonian of a spin system is in general well characterized, because the spin-exchange constants can be measured directly. The exchange between the spins would correspond to short-range interactions, leading to very good realization of some of the models of itinerant particles, for which the short range of the interaction is usually only an approximation. In that respect, quantum spin systems play a role similar to the one of cold atomic gases,[34] in connection with the question of itinerant interacting systems.

In this paper, we present a detailed calculation of the properties of weakly coupled spin-1/2 ladders. We focus in particular on their dynamics and their low-energy physics, providing a detailed analysis and a *quantitative* description necessary for an unbiased comparison with experiments. More precisely, we explore the phase diagram of such a system, computing static quantities (magnetization, specific heat, BEC critical temperature, order parameter) and the NMR relaxation rate, by using a combination of analytic [mostly LL theory and a Bethe ansatz (BA)] and numerical [mostly density-matrix renormalization group (DMRG) and quantum Monte Carlo (QMC)] techniques. We compare our results with the various measurements on the compound BPCB. A short account of some of these results in connection with measurements on BPCB was previously published in Refs. 29–31. Here we extend these results and give the details on how the theoretical results were obtained. Motivated by recent experimental measurements, we further investigate the excitation spectra and dynamical correlation functions at high and intermediate energies, for which a theoretical description is very challenging. We show how for the low-energy part of the spectrum it is possible to use the mapping to low-energy effective theories, such as the LL or to a spin chain, which can be solved by BA techniques.[35,36] Such a technique does not work, however, for energies of the order of the magnetic exchange of the system. In this paper we thus complement such analytical approaches by a DMRG analysis. We use the recent real-time variant to obtain the dynamics[37–40] in real time and the dynamical correlation functions. The same technique can be used also to obtain finite-temperature results.[41–43] This allows to obtain an accurate computation of the excitation spectra and correlation functions in the high-energy regime. We use different analytical approaches to interpret our numerical results.

The paper is structured as follows. Section II defines the model of weakly coupled spin ladders. Its basic excitations and phase diagram are introduced as well as the spin chain mapping, which proves to be very helpful for the physical interpretations. Section III briefly recalls the different analytical (LL, BA) and numerical (DMRG, QMC) techniques that we used to obtain the results described in the present paper. Section IV gives a detailed characterization of the phase diagram, focusing on the static properties and the NMR relaxation rate. Section V presents the computed dynamical correlations of a single spin ladder at different magnetic fields and couplings. The numerical calculations are compared to previous results (link cluster expansion, spin chain mapping, weak coupling approach) and analytical descriptions (LL, *t-J* model). Section VI compares directly the computed quantities to experimental measurements. In particular, the theoretical spectra are compared to the low-energy INS measurements on the compound BPCB. It also provides predictions for the high-energy part of the INS cross section. Finally, Sec. VII summarizes our conclusions and discusses further perspectives.

II. COUPLED SPIN-1/2 LADDERS

In this section we introduce the theoretical model of weakly coupled spin-1/2 ladders in a magnetic field. We recall its low-temperature phase diagram, paying special attention to the regime of strong coupling along the rungs of the ladder. This regime is particularly interesting because it is realized in the spin-ladder compound $(\mathrm{C}_5\mathrm{H}_{12}\mathrm{N})_2\mathrm{CuBr}_4$, customarily called BPCB. We discuss briefly the energy scales for BPCB in the present section, leaving more detailed discussions for Sec. VI.

A. Model

The Hamiltonian we consider is

$$H_{3\mathrm{D}} = \sum_{\mu} H_{\mu} + J' \sum \mathbf{S}_{l,k,\mu} \cdot \mathbf{S}_{l',k',\mu'}. \tag{1}$$

Here H_μ is the Hamiltonian of the single ladder μ and J' is the strength of the interladder coupling. The operator $\mathbf{S}_{l,k,\mu} = (S^x_{l,k,\mu}, S^y_{l,k,\mu}, S^z_{l,k,\mu})$ acts at the site l $(l = 1,2,\ldots,L)$ of the leg k $(k = 1,2)$ of the ladder μ. Often we will omit ladder indices from the subscripts of the operators (in particular, we replace $\mathbf{S}_{l,k,\mu}$ with $\mathbf{S}_{l,k}$) to lighten notation. $S^\alpha_{l,k}$ $(\alpha = x,y,z)$

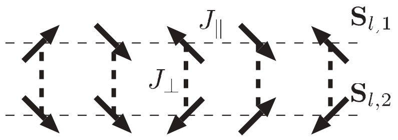

FIG. 1. Single ladder structure: $J_\perp$ ($J_\parallel$) is the coupling along the rungs (legs) represented by thick (thin) dashed lines and $\mathbf{S}_{l,k}$ are the spin operators acting on the site l of the leg $k = 1,2$.

are conventional spin-1/2 operators with $[S^x_{l,k},S^y_{l,k}] = iS^z_{l,k}$ and $S^\pm_{l,k} = S^x_{l,k} \pm iS^y_{l,k}$.

The Hamiltonian H_μ of the spin-1/2 two-leg ladder illustrated in Fig. 1 is

$$H_\mu = J_\perp H_\perp + J_\parallel H_\parallel, \tag{2}$$

where $J_\perp$ ($J_\parallel$) is the coupling constant along the rungs (legs) and

$$H_\perp = \sum_l \mathbf{S}_{l,1}\cdot\mathbf{S}_{l,2} - h^z J_\perp^{-1} M^z, \tag{3}$$

$$H_\parallel = \sum_{l,k} \mathbf{S}_{l,k}\cdot\mathbf{S}_{l+1,k}. \tag{4}$$

The magnetic field, h^z, is applied in the z direction, and M^z is the z component of the total spin operator $\mathbf{M} = \sum_l(\mathbf{S}_{l,1} + \mathbf{S}_{l,2})$. Since H_μ has the symmetry $h^z \to -h^z, M^z \to -M^z$, we only consider $h^z \geqslant 0$. The relation between h^z and the physical magnetic field in experimental units is given in Eq. (40).

B. Energy scales

In the present paper we focus on the case of spin-1/2 antiferromagnetic ladders that are weakly coupled to one another. This means that the interladder coupling $J' > 0$ is much smaller than the intraladder couplings $J_\parallel$ and $J_\perp$, i.e.,

$$0 < J' \ll J_\parallel \quad \text{and} \quad J_\perp. \tag{5}$$

As we will show, the model (1) accurately describes the magnetic properties of the compound BPCB. Its detailed description is given in Sec. VI. The couplings have been experimentally determined to be[30,31]

$$J' \approx 20\text{–}100\ \text{mK} \tag{6}$$

and[30]

$$J_\parallel \approx 3.55\ \text{K}, \quad J_\perp \approx 12.6\ \text{K}. \tag{7}$$

More details about the determination of the couplings for the compound BPCB are given in Sec. VI.

C. Spin ladder to spin chain mapping

The physical properties of a single ladder (2) are defined by the value of the dimensionless coupling

$$\gamma = \frac{J_\parallel}{J_\perp}. \tag{8}$$

In the limit $J_\parallel = 0$ (therefore $\gamma = 0$), the rungs of the ladder are decoupled. Hereafter we refer to this as the *decoupled bond limit*. The four eigenstates of each decoupled rung are as follows: the singlet state

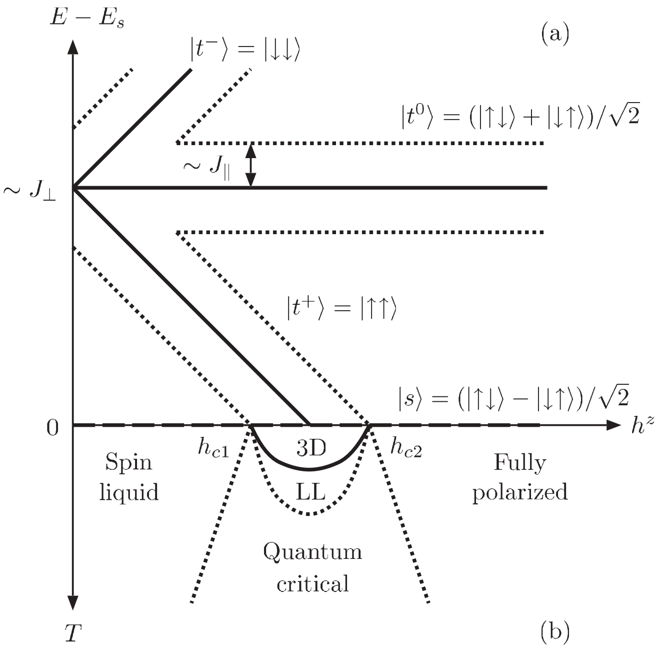

FIG. 2. (a) Energy of the triplets $|t^+\rangle$, $|t^0\rangle$, $|t^-\rangle$ (solid lines) and singlet $|s\rangle$ (dashed line) vs the applied magnetic field in the absence of an interrung coupling ($J_\parallel = 0$). The dotted lines represent the limits of the triplet excitation band when $J_\parallel \neq 0$. (b) Phase diagram of weakly coupled spin ladders: Crossovers (dotted lines) and the phase transition (solid line) that only exists in the presence of an interladder coupling are sketched.

$$|s\rangle = \frac{|\uparrow\downarrow\rangle - |\downarrow\uparrow\rangle}{\sqrt{2}}, \tag{9}$$

with the energy $E_s = -3J_\perp/4$, spin $S = 0$, and z projection of the spin $S^z = 0$, and three triplet states

$$|t^+\rangle = |\uparrow\uparrow\rangle, \quad |t^0\rangle = \frac{|\uparrow\downarrow\rangle + |\downarrow\uparrow\rangle}{\sqrt{2}}, \quad |t^-\rangle = |\downarrow\downarrow\rangle, \tag{10}$$

with $S = 1$, $S^z = 1,0,-1$, and energies $E_{t^+} = J_\perp/4 - h^z$, $E_{t^0} = J_\perp/4$, $E_{t^-} = J_\perp/4 + h^z$, respectively. The ground state is $|s\rangle$ below the critical value of the magnetic field, $h_c^{\text{DBL}} = J_\perp$, and $|t_+\rangle$ above. The dependence of the energies on the magnetic field is shown in Fig. 2(a).

A small but finite $\gamma > 0$ delocalizes triplets and creates bands of excitations with a bandwidth $\sim J_\parallel$ for each triplet branch. This leads to three distinct phases in the ladder system (2) depending on the magnetic field:

(i) *Spin liquid phase* (this phase is also called the *quantum disordered phase*[5]), which is characterized by a spin-singlet ground state (see Sec. IV A) and a gapped excitation spectrum (see Sec. V B). This phase appears for magnetic fields ranging from 0 to h_{c_1}.

(ii) *Gapless phase,* which is characterized by a gapless excitation spectrum. It occurs between the critical fields h_{c_1} and h_{c_2}. The ground-state magnetization per rung, $m^z = \langle M^z\rangle/L$, increases from 0 to 1 for h^z running from h_{c_1} to h_{c_2}. The low-energy physics can be described by the LL theory (see Sec. III C).

(iii) *Fully polarized phase,* which is characterized by the fully polarized ground state and a gapped excitation spectrum. This phase appears above h_{c2}.

Besides ladders, the transition between (i) and (ii) can occur in several other gapped systems such as the Haldane $S = 1$ chains or frustrated chains.[19,44–46] In the gapless phase, the distance between the ground state and the bands $|t^0\rangle$ and $|t^-\rangle$, which is of the order of $J_\perp$, is much larger than the width of the band $|t^+\rangle \sim J_\parallel$, because $\gamma \ll 1$.

For small γ the ladder problem can be reduced to a simpler spin chain problem. The essence of the *spin chain mapping*[2,17,47,48] is to project out $|t^0\rangle$ and $|t^-\rangle$ bands from the Hilbert space of the model (2). The remaining states $|s\rangle$ and $|t^+\rangle$ are identified with the spin states

$$|\tilde{\downarrow}\rangle = |s\rangle, \quad |\tilde{\uparrow}\rangle = |t^+\rangle. \tag{11}$$

The local spin operators $\mathbf{S}_{l,k}$ therefore can be identified in the reduced Hilbert space spanned by the states (11) with the new effective spin-1/2 operators $\tilde{\mathbf{S}}_l$:

$$S^{\pm}_{l,k} = \frac{(-1)^k}{\sqrt{2}}\tilde{S}^{\pm}_l, \quad S^z_{l,k} = \frac{1}{4}\left(1 + 2\tilde{S}^z_l\right). \tag{12}$$

The Hamiltonian (2) reduces to the Hamiltonian of the spin-1/2 *XXZ* Heisenberg chain,

$$\begin{aligned} H_{XXZ} \;=\; & J_\parallel \sum_l \left(\tilde{S}^x_l \tilde{S}^x_{l+1} + \tilde{S}^y_l \tilde{S}^y_{l+1} + \Delta \tilde{S}^z_l \tilde{S}^z_{l+1}\right) \\ & - \tilde{h}^z \tilde{M}^z + L\left(-\frac{J_\perp}{4} + \frac{J_\parallel}{8} - \frac{h^z}{2}\right). \end{aligned} \tag{13}$$

Here the pseudospin magnetization is $\tilde{M}^z = \sum_l \tilde{S}^z_l$, the magnetic field $\tilde{h}^z = h^z - J_\perp - J_\parallel/2$, and the anisotropy parameter

$$\Delta = \tfrac{1}{2}. \tag{14}$$

Note that the spin chain mapping constitutes a part of a more general strong coupling expansion of the model (2), as discussed in Appendix A.

For the compound BPCB the parameter γ is rather small,

$$\gamma \approx \tfrac{1}{3.55} \approx 0.282, \tag{15}$$

and the spin chain mapping (13) gives the values of many observables fairly well. Some important effects are, however, not captured by this approximation. Examples will be given in later sections.

D. Role of weak interladder coupling

Let us now turn back to the more general Hamiltonian (1) and discuss the role of a weak interladder coupling J' [couplings ordered as in Eq. (5)]. The spin liquid and fully polarized phases are almost unaffected by the presence of J' whenever the gap in the excitation spectrum is larger than J' (see, e.g., Ref. 18 for more details). However, a new three-dimensional (3D) antiferromagnetic order in the plane perpendicular to h^z emerges in the gapless phase for $T \lesssim J'$. The corresponding phase, called *3D-ordered*, shows up at low enough temperatures T_c in numerous experimental systems with reduced dimensionality and a gapless spectrum.[5] For the temperature $T \gtrsim J'$ the ladders decouple from each other and the system undergoes a deconfinement transition into a LL regime (which will be described in Sec. III C). For $T \gtrsim J_\parallel$ the rungs decouple from each other and the system becomes a (quantum-disordered) paramagnet. All of the above-mentioned phases are illustrated in Fig. 2(b).

III. METHODS

In this section, we present the methods used to study the ladder system and its mean-field extension to the case of weakly coupled ladders. We first focus on the so-called DMRG or matrix product state (MPS) methods. These numerical methods allow us to investigate dynamical correlations at zero and finite temperature. Additionally, we discuss the BA used to obtain properties of the system after the spin chain mapping. Furthermore, we introduce an analytical low-energy description for the gapless phase, the LL theory. This theory, in combination with a numerical determination of its parameters (see Appendix B), gives a quantitative description of the low-energy physics. Finally, we treat the weak interladder coupling J' by a mean-field approach, both analytically and numerically, and a QMC technique.

A. DMRG

A numerical method used to determine static and dynamical quantities at zero and finite temperature of a quasi1D system is the DMRG. This method was originally introduced by White[49] to study static properties of 1D systems. Since usually the dimension of the total Hilbert space of a many-body quantum system is too large to be treated exactly, the main idea of the DMRG algorithm is to describe the important physics by using a reduced effective space. This reduced effective space is chosen optimally by using a variational principle. The DMRG has been proven very successfully in many situations and has been generalized to compute dynamical properties of quantum systems by using different approaches in frequency space.[50–52] Recently the interest in this method even increased after a successful generalization to time-dependent phenomena and finite-temperature situations.[37–43] The real-time calculations give an alternative route to determine dynamical properties of the system[38] that we use in the following. An overview of the method, its extensions, and its successful applications to real-time and finite temperature can be found in Refs. 50 and 51. Further details on the method and its technical aspects are given in Appendix C.

B. Bethe ansatz (BA)

The spin-1/2 *XXZ* chain (13), which is obtained after the spin chain mapping of the system is exactly solvable: The so-called BA technique gives explicit analytic expressions for its eigenfunctions and spectrum.[53,54] To convert this information into a practical recipe of calculation of the correlation functions is a highly sophisticated problem. However, a known solution to this problem (Ref. 35 and references therein) incorporates involved analytics and numerics, the latter limiting the precision of the final results to approximately the same extent as to-date implementations of the DMRG method. Calculation of the thermodynamic properties of the spin-1/2 *XXZ* chain model (13) by the BA technique is a simpler, but still nontrivial, task, requiring a solution of an infinite set of nonlinear coupled integral equations.[55] The solution of such equations can be only found numerically, and already in the 1970s this was done with a high precision.[56]

Later on, an alternative to the BA, the quantum transfer-matrix method, was used to obtain the thermodynamics of the *XXZ* chain in a magnetic field.[57] Within this approach the free energy of the system is expressed through the largest eigenvalue of the transfer matrix. This largest eigenvalue is given by the solution of a set of nonlinear equations [see Eq. (66.a) of Ref. 57], which are written in a form very suitable for solving them iteratively. In the present paper we followed this route and obtained the results for the specific heat for all temperatures and various magnetic fields with very high precision (see Sec. IV B 2).

C. Luttinger liquid (LL)

The LL Hamiltonian governs the dynamics of the free bosonic excitations with linear spectrum and can be written as[6,7]

$$H_{\rm LL} = \frac{1}{2\pi}\int dx \left\{ uK[\partial_x\theta(x)]2 + \frac{u}{K}[\partial_x\phi(x)]^2 \right\}, \qquad (16)$$

where ϕ and θ are canonically commuting bosonic fields, $[\phi(x),\partial_y\theta(y)] = i\pi\delta(x-y)$. The dimensionless parameter K entering Eq. (16) is customarily called the LL parameter, and u is the propagation velocity of the bosonic excitations (velocity of sound). Many 1D interacting quantum systems belong to the LL universality class: The dynamics of their low-energy excitations is governed by the Hamiltonian (16) and the local operators are written through the free boson fields θ and ϕ (the latter procedure if often called bosonization).

The spin-1/2 *XXZ* Heisenberg chain, Eq. (13), in the gapless phase is a well-known example of a model belonging to the LL universality class. Its local operators are expressed through the boson fields as follows:[6]

$$\tilde{S}^{\pm}(x) = e^{\mp i\theta(x)}\{\sqrt{2A_x}(-1)^x + 2\sqrt{B_x}\cos[2\phi(x) - 2\pi\tilde{m}^z x]\} \qquad (17)$$

and

$$\tilde{S}^z(x) = \tilde{m}^z - \frac{\partial_x\phi(x)}{\pi} + \sqrt{2A_z}(-1)^x\cos[2\phi(x) - 2\pi\tilde{m}^z x]. \qquad (18)$$

Here the continuous coordinate $x = la$ is given in units of the lattice spacing a, $\tilde{m}^z = \langle\tilde{M}^z\rangle/L$ is the magnetization per site of the spin chain, and A_x, B_x, and A_z are coefficients that depend on the parameters of the model (13). How to calculate K, u, A_x, B_x, and A_z is described in Appendix B 1.

The Hamiltonian (13) is the leading term in the strong coupling expansion (the parameter $\gamma = J_\parallel/J_\perp \ll 1$; see Appendix A) of the model (2). The local operators of the latter model are bosonized by combining Eqs. (12), (17), and (18). The analysis of the model (2) suggests[2,19,20] that the bosonization of the local spins can be performed for *any* values of $J_\perp$ and $J_\parallel$ in the gapless regime. We would like to stress that even for a small γ some parameters out of K, u, A_x, B_x, and A_z show significant numerical differences if calculated within the spin chain (13) compared to the spin ladder (2). We discuss this issue in Appendix B 1.

D. Mean-field approximation

Up to now, we have presented methods adapted to deal with 1D systems. In real compounds, an interladder coupling is typically present. As discussed in Sec. II D, in the incommensurate regime this interladder coupling J' [cf. Eq. (1)] can lead to a new 3D order [3D-ordered phase in Fig. 2(b)] at temperatures of the order of the coupling J'. In the case of BPCB, the interladder coupling is much smaller than the coupling inside the ladders, i.e., $J' \ll J_\perp, J_\parallel$ (Sec. VI A). Therefore, unless one is extremely close to h_{c1} or h_{c2}, one can treat the interladder coupling with a standard mean-field approximation. This approach incorporates all the fluctuations inside a ladder. However, it overestimates the effect of J' by neglecting quantum fluctuations between different ladders. Such effects can be taken partly into account by a suitable change of the interladder coupling,[31] which will be discussed in Sec. IV D. Close to the critical fields, the interladder coupling J' becomes larger than the effective energy of the 1D system. This forces one to consider a 3D approach from the start and brings the physics of the system in the universality class of BEC.[2,5] In the following, we consider that we are far enough (i.e., by an energy of the order of J') away from the critical points so that we can use the mean-field approximation.

Since the single ladder correlation functions along the magnetic-field direction (z axis) decay faster than the staggered part of the ones in the perpendicular xy plane [see Eqs. (B2) and (B3) for the LL exponent K of the ladder shown in Fig. 23], the 3D order will first occur in this plane. Thus the dominant order parameter is the $q = \pi$ staggered magnetization perpendicular to the applied magnetic field. The mean-field decoupling of the spin operators of neighboring ladders thus reads

$$S^x_{l,k} \cong -(-1)^{l+k}m^x_a \Rightarrow m^x_a = -(-1)^{l+k}\langle S^x_{l,k}\rangle, \qquad (19)$$

$$S^z_{l,k} \cong \frac{m^z}{2} - (-1)^{l+k}m^z_a. \qquad (20)$$

We have chosen the xy ordering to be along the x axis, and m^z_a will be very small and therefore neglected.

This approximation applied on the interladder interaction part of the 3D Hamiltonian $H_{\rm 3D}$ [Eq. (1)] leads to

$$H_{\rm MF} = J_\parallel H_\parallel + J_\perp H_\perp + \frac{n_c J' m^z}{4}\sum_{l,k} S^z_{l,k} + \frac{n_c J' m^x_a}{2}\sum_{l,k}(-1)^{l+k}S^x_{l,k}. \qquad (21)$$

Here we assume that the coupling is dominated by n_c neighboring ladders, where n_c is the rung connectivity ($n_c = 4$ for the case of BPCB; cf. Fig. 18). This mean-field Hamiltonian corresponds to a single ladder in a site-dependent magnetic field with a uniform component in the z direction and a staggered component in the x direction. The ground-state wave function of the Hamiltonian must be determined, fulfilling the self-consistency condition for m^z and m^x_a, by using numerical or analytical methods. This amounts to minimize the ground-state energy of some variational Hamiltonian.

1. Numerical mean field

The order parameters m^z and m_a^x can be computed numerically by treating the mean-field Hamiltonian H_{MF} self-consistently with DMRG. These parameters are evaluated recursively in the middle of the ladder (to minimize the boundary effects) starting with $m^z = 0$ and $m_a^x = 0.5$. An accuracy of $<10^{-3}$ on these quantities is reached quickly after a few recursive iterations (typically $\sim$5) of the DMRG, keeping a few hundred DMRG states and treating a system of length $L = 150$. We verified by keeping as well the alternating part of the z-order parameter m_a^z that this term is negligible ($<10^{-5}$).

2. Analytical mean field

Using the low-energy LL description of our ladder system (see Sec. III C), it is possible to treat the mean-field Hamiltonian H_{MF} within the bosonization technique. Introducing the LL operators (17) and (18) in H_{MF} (21) and keeping only the most relevant terms leads to the Hamiltonian[58,59]

$$H_{\mathrm{SG}} = \frac{1}{2\pi}\int dx\left\{uK[\partial_x\theta(x)]^2 + \frac{u}{K}[\partial_x\phi(x)]^2\right\} + \sqrt{A_x}n_c J' m_a^x \int dx \cos[\theta(x)], \tag{22}$$

where we neglected the mean-field renormalization of h^z in (21). This Hamiltonian differs from the standard LL Hamiltonian H_{LL} (16) by a cosine term corresponding to the x-staggered magnetic field in (21). It is known as the sine-Gordon Hamiltonian.[6,60,61] The expectation values of the fields can be derived from integrability.[62] In particular, m_a^x can be determined self-consistently.

E. Quantum Monte Carlo (QMC)

In order to take into account the detailed coupling structure of the BPCB compound shown in Fig. 18, which is neglected in the mean-field approximation (Sec. III D), we employ a stochastic series expansion implementation of the QMC technique with directed loop updates[63] provided with the Algorithms and Libraries for Physics Simulations (ALPS) libraries.[64,65] Nevertheless, due to the strong anisotropy of the couplings (5), the temperatures at which the effects of the interladder coupling J' become visible are not reachable with this method. The QMC results for the transition temperature of the 3D-ordered phase, T_c, presented in Ref. 31, Sec. IV D 1, and Appendix D are then computed with a J' of $\sim$3 times larger than that extracted in Ref. 30 and Sec. IV D 1, making the 3D effects numerically accessible.

IV. STATIC PROPERTIES AND NMR RELAXATION RATE

We begin our analysis of the different phases of the coupled spin ladder system [Fig. 2(b)] by computing thermodynamic quantities, such as the magnetization, the rung state density, and the specific heat. In particular, we test the LL low-energy prediction of the latter and evaluate the related crossover to the quantum critical regime. Furthermore, we discuss the effect of the 3D interladder coupling by computing the staggered magnetization in the 3D-ordered phase and its critical temperature. We finally discuss the NMR relaxation rate in the gapless regime related to the low-energy dynamics. In order to compare these physical quantities to the experiments, all of them are computed for the BPCB parameters (see Sec. VI A).

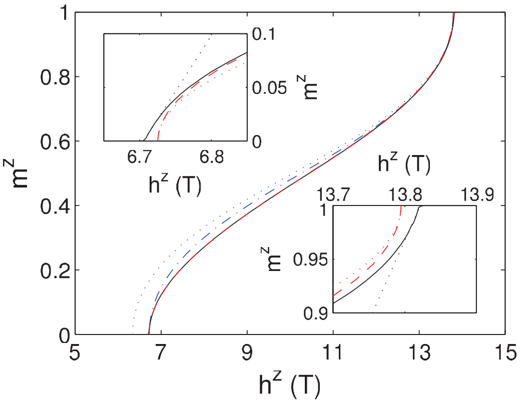

FIG. 3. (Color online) Dependence of the magnetization per rung m^z on the magnetic field h^z at zero temperature for the single ladder with the BPCB couplings (see Sec. VI A) (dashed red line), the spin chain mapping (dotted blue line) rescaled to fit with the single ladder critical fields (dashed-dotted blue line), and for the weakly coupled ladders treated by the mean-field approximation (solid black line). The insets emphasize the different behavior of the magnetization curves for the single (dashed red line) and coupled (solid black line) ladders close to the critical fields, which are indistinguishable in the main part of the figure. The dotted lines in the insets correspond to the linear and square-root-like critical behavior.

A. Critical fields

The zero-temperature magnetization contains extremely useful information. Its behavior gives directly the critical values of the magnetic fields h_{c1} and h_{c2} at which the system enters and leaves the gapless regime, respectively [Fig. 2(b)]. In Fig. 3 the dependence of the magnetization on the applied magnetic field is shown for a single ladder and for the weakly coupled ladders. At low magnetic field, $h^z < h_{c1}$, the system is in the gapped spin liquid regime with zero magnetization, and spin singlets on the rungs dominate the behavior of the system[66] (see Fig. 4). At $h^z = h_{c1}$, the Zeemann interaction closes the spin gap to the rung triplet band $|t^+\rangle$ (Fig. 2). Above $h^z > h_{c1}$, the triplet $|t^+\rangle$ band starts to be populated, leading to an increase of the magnetization with h^z. The lower critical field in a 13th-order expansion[10] in γ is $h_{c1} \approx 6.73$ T for the BPCB parameters. At the same time the singlet and the high-energy triplet occupation decreases (Fig. 4). For $h^z > h_{c2} = J_\perp + 2J_\parallel \approx 13.79$ T (for the compound BPCB), the $|t^+\rangle$ band is completely filled and the other bands are depopulated. The system becomes fully polarized ($m^z = 1$) and gapped. The two critical fields, h_{c1} and h_{c2}, are closely related to the two ladder exchange couplings, $J_\perp$ and $J_\parallel$. As they are experimentally easily accessible, assuming that a ladder Hamiltonian is an accurate description of the system, these critical fields can be used to determine the ladder couplings.[30]

Such a general behavior of the magnetization is seen for both the single ladder and the weakly coupled ladders in Fig. 3. In particular, the effect of a small coupling J' between the ladders is completely negligible in the central part of the curve. Only in the vicinity of the critical fields, the single

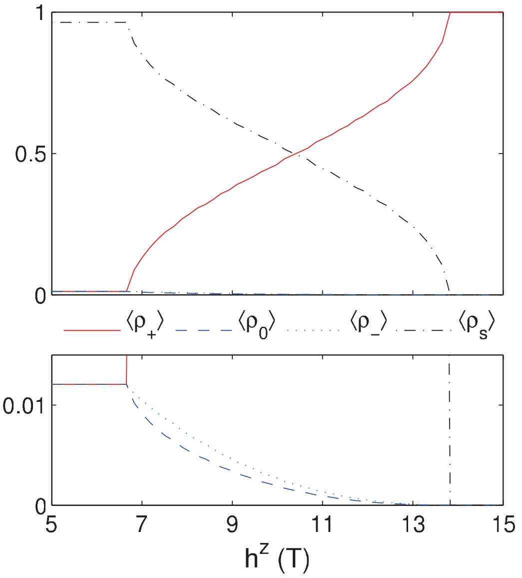

FIG. 4. (Color online) Rung state density vs the applied magnetic field h^z at zero temperature for the single ladder with the BPCB couplings (zero-temperature DMRG calculations averaging on the central sites of the ladder). The dashed-dotted (black) lines correspond to the singlet density $\langle \rho_s \rangle$. The triplet densities are represented by the solid (red) lines for $\langle \rho_+ \rangle$, the dashed (blue) lines for $\langle \rho_0 \rangle$, and the dotted (green) lines for $\langle \rho_- \rangle$.

ladder and the coupled ladders show a distinct behavior. The single ladder behaves as an empty (filled) 1D system of noninteracting fermions, which leads to a square-root behavior $m^z \propto (h^z - h_{c1})^{1/2}$ close to the lower critical field and $1 - m^z \propto (h_{c2} - h^z)^{1/2}$ close to the upper critical field. In contrast, in the system of weakly coupled ladders, a 3D-ordered phase appears at low enough temperatures in the gapless regime (see Secs. II D and III D). The magnetization dependence close to the critical fields becomes linear, $m^z \propto h^z - h_{c1}$ and $1 - m^z \propto h_{c2} - h^z$, respectively.[2,46] In comparison with the single ladder, the critical fields given above are shifted by a value of the order of J'. This behavior is in the universality class of the BEC and is well reproduced by the mean-field approximation, as shown in the insets of Fig. 3 close to the critical fields.

For comparison, the magnetization of a single ladder in the spin chain mapping is also plotted in Fig. 3. This approximation reproduces well the general behavior of the ladder magnetization discussed above. However, note that for the exchange coupling constants considered here, the lower critical field in this approximation is different from the ladder one. The lower critical field is $h_{c1}^{XXZ} = J_\perp - J_\parallel \approx 6.34\,\mathrm{T} < h_{c1}$. The upper critical field $h_{c2}^{XXZ} = J_\perp + 2J_\parallel = h_{c2}$ is the same as for the ladder. If we rescale h_{c1}^{XXZ} and h_{c2}^{XXZ} to match the critical fields h_{c1} and h_{c2} $[\tilde{h}^z \rightarrow \frac{(\tilde{h}^z - h_{c1}^{XXZ})(h_{c2} - h_{c1})}{h_{c2}^{XXZ} - h_{c1}^{XXZ}} + h_{c1}]$, the magnetization curve gets very close to the one calculated for a ladder. However, in contrast to the magnetization curve for the ladder, the corresponding curve in the spin chain mapping is symmetric with respect to its center at $h_m^{XXZ} = \frac{h_{c1}^{XXZ} + h_{c2}^{XXZ}}{2} = J_\perp + J_\parallel/2$ due to the absence of the high-energy triplets.

B. The LL regime and its crossover to the critical regime

The thermodynamics of the spin-1/2 ladders has been studied in the past.[11,21,22,29] Here we summarize the main interesting features of the magnetization and the specific heat, focusing on the crossover between the LL regime and the quantum critical region, using the BPCB parameters (Sec. VI A). As the interladder exchange coupling J' is very small compared to the ladder exchange couplings $J_\parallel$ and $J_\perp$, it is reasonable to neglect it in this regime far from the 3D phase. Therefore we focus on a single ladder in the following.

1. Finite-temperature magnetization

We start the description of the temperature dependence of the magnetization in the two gapped regimes: the spin liquid phase and the fully polarized phase (not shown; cf. Refs. 21 and 23). For small magnetic fields $h^z < h_{c1}$, the magnetization vanishes exponentially at zero temperature and after a maximum at intermediate temperatures it decreases to zero for large temperatures. For large magnetic fields $h^z > h_{c2}$, the magnetization increases exponentially up to $m^z = 1$ at low temperature and decreases monotonously in the limit of infinite temperature.

In the gapless regime, the magnetization at low temperature has a nontrivial behavior that strongly depends on the applied magnetic field. The temperature dependence of the magnetization computed with the finite-temperature DMRG (T-DMRG) (see Appendix C 2) is shown in Fig. 5(a) for different values of the magnetic field in the gapless phase, $h^z = 9$, 10, and 11 T ($h_{c1} < h^z < h_{c2}$). In this regime new extrema appear in the magnetization at low temperature. This behavior can be understood close to the critical fields, where the ladder can be described by a 1D fermion model with negligible interaction between fermions. Indeed, in this simplified picture[6] and in more refined calculations[21,22,24] the magnetization has an extremum where the temperature reaches the chemical potential, i.e., at the temperature at which the energy of excitations starts to feel the curvature of the energy band. This specific behavior is illustrated in Fig. 5(a) with the curve for $h^z = 11$ T ($h_m = \frac{h_{c1}+h_{c2}}{2} < h^z < h_{c2}$). The low-temperature maximum moves to higher temperature for $h^z < h_m$ and goes over to the already discussed maximum for $h^z < h_{c1}$. Symmetrically with respect to h_m, a low-temperature minimum appears in the curve for $h^z = 9$ T ($h_{c1} < h^z < h_m$). This minimum slowly disappears for $h^z \rightarrow h_m$ (the curve for $h^z = 10$ T is close to that).

The location of the lowest extremum is a reasonable criterion to characterize the crossover temperature between the LL and the quantum critical regime,[21,22] because the extremum occurs at temperatures of the order of the chemical potential. A plot of this crossover temperature versus the magnetic field is presented in Fig. 5(c). Following this criterium, the crossover has a continuous shape far from h_m. Nevertheless, close to h_m, both extrema are close to each other (because the maximum still exists for $h^z < h_m$ field at which the minimum appears). The criterium is thus not well defined. It presents a discontinuity at h_m, which is obviously an artefact. In the vicinity of h_m, we thus use another crossover criterium based on the specific heat (see Sec. IV B 2) that seems to give a more accurate description. In Ref. 29, both criteria have been applied

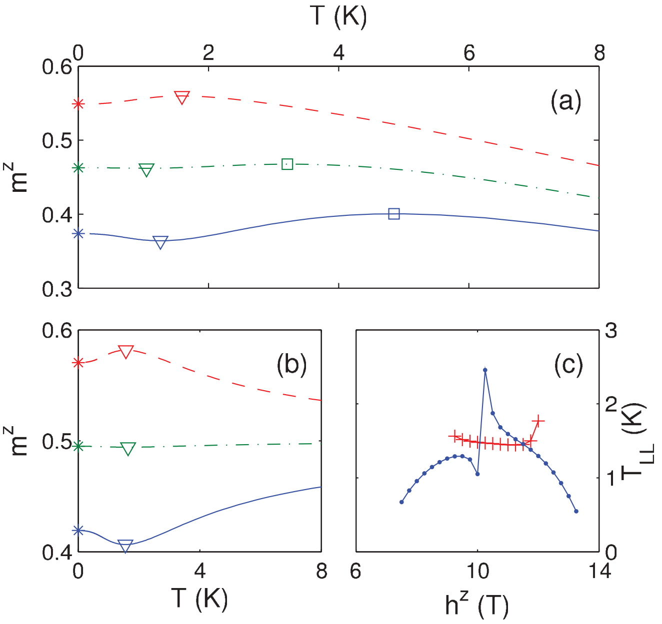

FIG. 5. (Color online) Temperature dependence of the magnetization per rung, $m^z(T)$, for (a) the ladder with the BPCB couplings (39) and (b) the spin chain mapping at different applied magnetic fields $h^z = 9$ T (solid blue lines), $h^z = 10$ T (dashed-dotted green lines), and $h^z = 11$ T (dashed red lines). The results were obtained using T-DMRG. The stars at $T = 0$ K are the ground-state magnetization per rung determined by zero-temperature DMRG. The triangles (squares) mark the low- (high-) energy extrema. (c) Crossover temperature T_{LL} of the LL to the quantum critical regime vs the applied magnetic field [blue dots for the extremum in $m^z(T)|_{h^z}$ criterium and red crosses for the maximum in $c(T)|_{h^z}$ criterium].

on the magnetocaloric effect and specific-heat measurements on the compound BPCB, and give a crossover temperature in agreement with the computed ones.

The temperature dependence of the magnetization of the spin chain mapping [Fig. 5(b)] exhibits a single low-temperature maximum if $h_m^{XXZ} < h^z < h_{c2}^{XXZ}$ (minimum if $h_{c1}^{XXZ} < h^z < h_m^{XXZ}$). The appearance of a single extremum and its convergence to $m^z \to 0.5$ when $T \to \infty$ is due to the exact symmetry with respect to the magnetic field h_m^{XXZ}. This approximation reproduces the main low-energy features of the ladder but fails to describe the high-energy behavior, which strongly depends on the high-energy triplets.

2. *Specific heat*

The specific heat has been investigated for similar parameters as the ones considered in this paper in the gapped and gapless regime in Refs. 21, 23, and 29. Here we concentrate on the detailed analysis in the gapless regime, in particular, on the low-temperature behavior and the determination of a crossover temperature from the first maximum. We show in Fig. 6 the typical temperature dependence of the specific heat for different values of the magnetic field. Comparisons with actual experimental data[29] for BPCB are excellent [see Fig. 6(b)]. For these comparisons the theoretical data are computed with $g = 2.06$ related to the experimental orientation of the sample with respect to the magnetic field[29] (see Sec. VI A) and rescaled by a factor 0.98, in agreement with the global experimental uncertainties.[67]

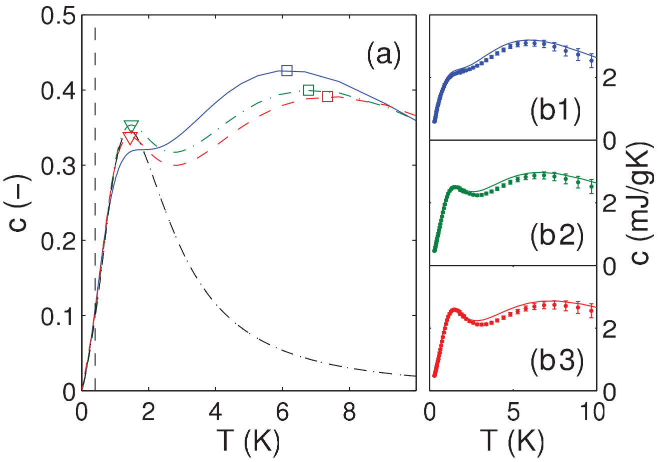

FIG. 6. (Color online) Specific heat per rung c vs the temperature T for different applied magnetic fields in the gapless regime. (a) Full ladder T-DMRG calculations with the BPCB couplings (39) for $h^z = 9$ T (solid blue line), $h^z = 10$ T (dashed-dotted green line), and $h^z = 11$ T (dashed red line). Spin chain mapping at $h^z = 10$ T solved by DMRG (dashed black line) and by BA (dotted black line). Note that the two lines are hardly distinguishable. The triangles (squares) mark the low- (high-) energy maxima of the specific heat vs temperature. The vertical dashed line marks the temperature $T = 0.4$ K below which the DMRG results are extrapolated (see Appendix C 2). (b) Comparison between measurements on the compound BPCB from Ref. 29 (dots) and the T-DMRG calculations[67] (solid lines) at (b1) $h^z = 9$ T, (b2) $h^z = 10$ T, and (b3) $h^z = 11$ T.

At low temperatures the specific heat has a contribution due to the gapless spinon excitations. This results in a peak $T \sim 1.5$ K. This peak is most pronounced for the magnetic-field values lying midvalue between the two critical fields. At higher temperatures the contribution of the gapped triplet excitations leads to a second peak, whose position depends on the magnetic field. To separate out the contribution from the low-lying spinon excitations, we compare the specific heat of the ladder to the results obtained by the spin chain mapping in which we just keep the lowest two modes of the ladder (see Sec. II C and Appendix A). The resulting effective chain model is solved using BA and T-DMRG methods. The agreement between these methods is excellent, and the corresponding curves in Fig. 6 are hardly distinguishable. However, a clear difference with the full spin ladder results is revealed. While at low temperatures the curves are very close, the first peak in the spin chain mapping already lacks some weight, which stems from higher modes of the ladder.

In Fig. 7 the low-temperature region is analyzed in more detail. At very low temperatures the spinon modes of the ladder can be described by the LL theory (see Sec. III C), which predicts a linear rise with temperature inversely proportional to the spinon velocity,[6,68]

$$c_{\mathrm{LL}}(T) = \frac{T\pi}{3u}. \tag{23}$$

In Fig. 7 we compare the results of the LL and the DMRG (and BA for the effective spin chain). The numerical results for the adaptive T-DMRG at finite temperature are extrapolated

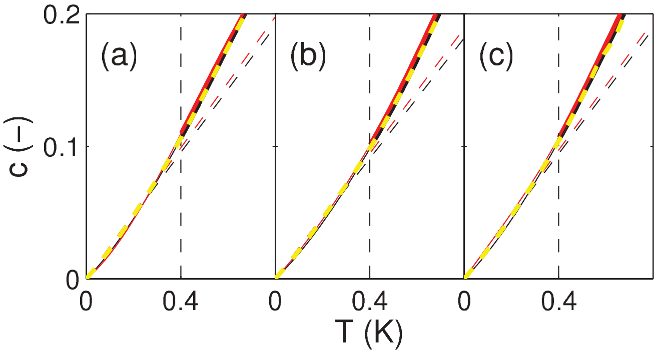

FIG. 7. (Color online) Low-temperature dependence of the specific heat per rung vs the temperature, $c(T)$, for (a) $h^z = 9$ T, (b) $h^z = 10$ T, and (c) $h^z = 11$ T. The T-DMRG calculations are shown as red thick lines for the ladder with the BPCB couplings (39) (black thick lines for the spin chain mapping). The two curves are hardly distinguishable. Their low-temperature polynomial extrapolation is plotted in thin lines below $T = 0.4$ K (represented by a vertical dashed line). The linear low-temperature behavior of the LL is represented by dashed lines (red for the ladder, black for the spin chain mapping). The dashed yellow lines correspond to the BA computation for the spin chain mapping.

to zero temperature by connecting algebraically to zero-temperature DMRG results (see Appendix C 2). A very good agreement between (23) and numerics is found for low temperatures. However, at higher temperatures, the slope of the $T \to 0$ LL description slightly changes with respect to the curves calculated with other methods. This change of slope reflects the fact that the curvature of the energy dispersion must be taken into account when computing the finite-temperature specific heat, even when the temperature is quite small compared to the effective energy bandwidth of the system. The effective spin chain and the numerical results for the ladder agree for higher temperatures (depending on the magnetic field), before the higher modes of the ladder cause deviations.

As for the magnetization (Sec. IV B 1), the location of the low-temperature peak can be interpreted as the crossover of the LL to the quantum critical regime. Indeed, in a free fermion description, which is accurate close to the critical fields, this peak appears at the temperature for which the excitations stem from the bottom of the energy band. The corresponding temperature crossover is compared in Fig. 5(c) to the crossover temperature extracted from the first magnetization extremum (Sec. IV B 1). The two crossover criteria are complementary due to their domain of validity. The first specific-heat maximum is well pronounced only in the center of the gapless phase. In contrast, in this regime the presence of two extrema close to each other in the magnetization renders the magnetization criterium very imprecise (cf. Sec. IV B 1).

C. Spin-lattice relaxation rate

As the spin-lattice relaxation in quantum spin systems is due to pure magnetic coupling between electronic and nuclear spins, the NMR spin-lattice relaxation rate T_1^{-1} is directly related to the local transverse correlation function[69] $\chi_a^{xx}(x=0,t)$ defined as in Eq. (B6),

$$T_1^{-1} = -\frac{T\gamma_n^2 A_\perp^2}{\omega_0}\mathrm{Im}\left[\int_{-\infty}^{\infty} dt\, e^{i\omega_0 t}\chi_a^{xx}(x=0,t)\right], \qquad (24)$$

where $T \gg \omega_0$ is assumed with the Larmor frequency ω_0. Here $\gamma_n = 19.3$ MHz/T is the nuclear gyromagnetic ratio of the measured nucleus (^{14}N in Ref. 30 for BPCB) and $A_\perp$ is the transverse hyperfine coupling constant.

Assuming $J_\parallel \gg T$, the T_1^{-1} due to the electronic spin dynamics can be computed in the gapless regime using the LL low-energy description. Following Ref. 2, we introduce the LL correlation (B7) into Eq. (24), and obtain

$$T_1^{-1} = \frac{\gamma^2 A_\perp^2 A_x \cos\left(\frac{\pi}{4K}\right)}{u}\left(\frac{2\pi T}{u}\right)^{\frac{1}{2K}-1} B\left(\frac{1}{4K}, 1-\frac{1}{2K}\right). \qquad (25)$$

According to the known LL parameters (Fig. 23) the shape of $T_1^{-1}(h_z)$ plotted in Fig. 8 at $T = 250$ mK $\gg T_c$ is strongly asymmetric with respect to the middle of the gapless phase. The only free (scaling) parameter, $A_\perp = 0.057$ T, is deduced from the fit of Eq. (25) to the experimental data[30] and agrees with other measurements. For comparison, the T_1^{-1} obtained in the spin chain mapping approximation is also plotted in Fig. 8. As for other physical quantities, this description fails to reproduce the nonsymmetric shape.

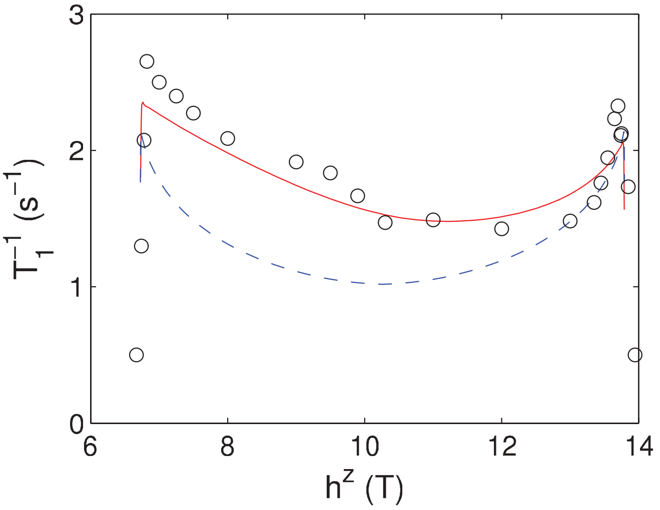

FIG. 8. (Color online) Magnetic-field dependence of the NMR relaxation rate, $T_1^{-1}(h^z)$, at $T = 250$ mK. The solid red line is the bosonization determination using the ladder LL parameters for the BPCB couplings (the dashed blue line uses the LL parameters of the spin chain mapping). The black circles are the measurements from Ref. 30.

D. Properties of weakly coupled ladders

The interladder coupling J' induces a low-temperature ordered phase [the 3D-ordered phase in Fig. 2(b)]. Using the mean-field approximation presented in Sec. III D, we characterize the ordering and compute the critical temperature and the order parameter related to this phase.

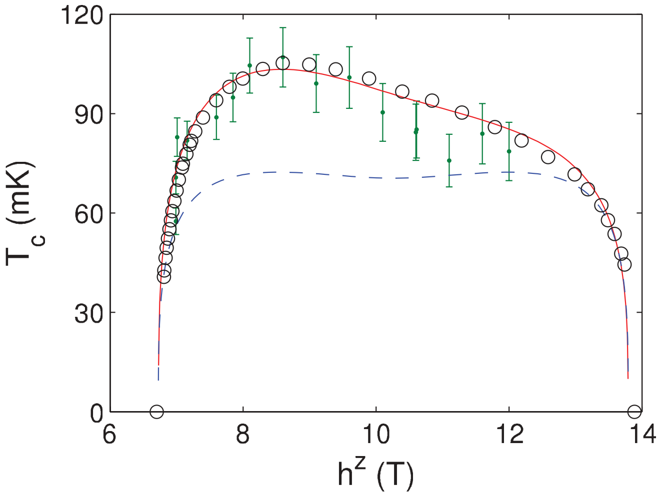

FIG. 9. (Color online) Magnetic-field dependence of the transition temperature between the gapless regime and the 3D-ordered phase, $T_c(h^z)$, is plotted as a solid red line for the ladder LL parameters of BPCB (dashed blue line for the LL parameters of the spin chain mapping). The NMR measurements from Ref. 30 are represented by black circles and the ND measurements from Ref. 31 are represented by green dots.

1. *3D-order transition temperature*

In order to compute the critical temperature of the 3D transition, we follow Ref. 2 and treat the staggered part of the mean-field Hamiltonian $H_{\rm MF}$ (21) perturbatively by using linear response. The instability of the resulting mean-field susceptibility, due to the 3D transition, appears at T_c when[71]

$$\chi_a^{xx}(q=0,\omega=0)|_{T_c} = -\frac{2}{n_c J'}, \tag{26}$$

where χ_a^{xx} is the transverse staggered retarded correlation function of an isolated single ladder system (see Appendix B 3). This correlation can be computed analytically [see Eq. (B8)] by using the LL low-energy description of the isolated ladder [Eq. (16)] in the gapless regime. Applying condition (26) to the LL correlation (B8) leads to the critical temperature,

$$T_c = \frac{u}{2\pi}\left[\frac{A_x J' n_c \sin\left(\frac{\pi}{4K}\right) B^2\left(\frac{1}{8K}, 1-\frac{1}{4K}\right)}{2u}\right]^{\frac{2K}{4K-1}}. \tag{27}$$

Introducing the computed LL parameters u, K, and A_x (see Fig. 23) in this expression, we obtain the critical temperature[30] as a function of the magnetic field. This is shown in Fig. 9 together with the experimental data. This allows us to extract the *mean-field* interladder coupling $J'_{\rm MF} \approx 20$ mK for the experimental compound BPCB [the *only* free (scaling) parameter in Eq. (27)]. The asymmetry of the LL parameters induces a strong asymmetry of T_c with respect to the middle of the 3D phase.

As the mean-field approximation neglects the quantum fluctuations between the ladders, the critical temperature T_c is overestimated for a given $J'_{\rm MF}$. We thus performed a QMC determination of this quantity based on the same 3D lattice structure. Let us note that QMC simulations of the coupled spin ladder Hamiltonian (1) are possible, because the 3D lattice structure (see Fig. 18) is unfrustrated. In Appendix D we present results on how to determine the critical temperatures for the 3D ordering transition by using QMC. This determination shows[31] that the real critical temperature is well approximated by the mean-field approximation, but with a rescaling of the real interladder coupling $J' \approx 27$ mK $= \alpha^{-1} J'_{\rm MF}$, with $\alpha \approx 0.74$. The rescaling factor α is similar to the values obtained for other quasi-1D antiferromagnets.[71,72]

2. *Zero-temperature 3D order parameter*

The staggered order parameter in the 3D-ordered phase, m_a^x, can be analytically determined at zero temperature by using the mean-field approximation for the interladder coupling and the bosonization technique (see Sec. III D). As $m_a^x = \sqrt{A_x}\langle\cos[\theta(x)]\rangle$ in the bosonization description and the expectation value[62] of the operator $e^{i\theta(x)}$ is

$$\langle e^{i\theta(x)}\rangle = \sqrt{A_x}F(K)\left(\frac{\pi\sqrt{A_x}n_c J' m_a^x}{2u}\right)^{\frac{1}{8K-1}} \tag{28}$$

for the sine-Gordon Hamiltonian $H_{\rm SG}$ (22) with

$$F(K) = \frac{\frac{\pi^2}{\sin\left(\frac{\pi}{8K-1}\right)}\frac{8K}{8K-1}\left[\frac{\Gamma\left(1-\frac{1}{8K}\right)}{\Gamma\left(\frac{1}{8K}\right)}\right]^{\frac{8K}{8K-1}}}{\left[\Gamma\left(\frac{4K}{8K-1}\right)\Gamma\left(\frac{16K-3}{16K-2}\right)\right]^2}, \tag{29}$$

we can extract

$$m_a^x = \sqrt{A_x}F(K)^{\frac{8K-1}{8K-2}}\left(\frac{\pi n_c A_x J'}{2u}\right)^{\frac{1}{8K-2}}. \tag{30}$$

This can be evaluated in the 3D-ordered phase by introducing into (30) the LL parameters u, K, and A_x from Fig. 23. Figure 10 shows the order parameter versus the magnetic field determined analytically and numerically by DMRG (see Sec. III D 1). The two curves are almost indistinguishable and exhibit a strongly asymmetric camel-like shape[30] with two maxima close to the critical fields. The asymmetry of the curve is again due to the presence of the additional triplet states. This asymmetry disappears in the spin chain mapping.

V. DYNAMICAL CORRELATIONS OF A SINGLE LADDER

In the next paragraph, we discuss the possible excitations and the corresponding correlation functions created by the spin operators. Such dynamical correlations allow us to study the excitations of our system. They are also directly related to many experimental measurements (NMR, INS, etc.). We first focus on the gapped spin liquid and then treat the gapless regime for fields $h_{c1} < h^z < h_{c2}$ [see Fig. 2(b)]. All correlations are computed by using the time-dependent DMRG (*t*-DMRG) at zero temperature for the single ladder (Appendix C 1), and are compared to analytical results when such results exist. In particular, we check the overlap with the LL description at low energy and use a strong coupling expansion (Appendix A) to qualitatively characterize the obtained spectra. We start with a discussion of the correlations for the parameters of the compound BPCB (see Sec. VI A), and then turn to the evolution of the spectra with the coupling ratio γ from the weak coupling ($\gamma \to \infty$) to strong coupling ($\gamma \approx 0$).

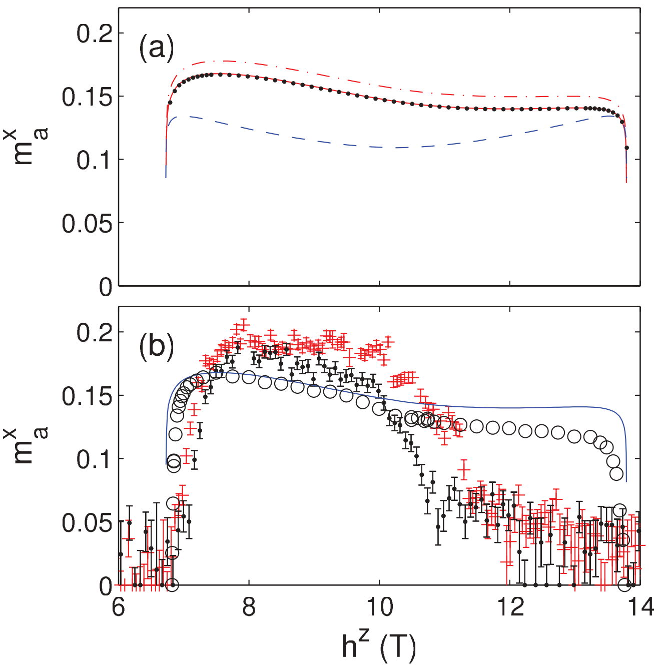

FIG. 10. (Color online) Magnetic-field dependence of the staggered magnetization per spin, $m_a^x(h^z)$, in the 3D-ordered phase determined for the ground state. (a) Its computation with the analytical bosonization technique for the LL parameters of the compound BPCB and $J' = 27$ mK is represented by the dashed-dotted red line (dashed blue line for the LL parameters of the spin chain mapping). The DMRG result for $J' = 20$ mK($=J'_{\mathrm{MF}}$) is represented by black dots (as a comparison, the bosonization result for $J' = 20$ mK is plotted as a solid red line). Note that these two data are almost indistinguishable. (b) Comparison between NMR measurements (black circles) done at $T = 40$ mK from Ref. 30 and scaled on the theoretical results for $J' = 27$ mK, ND measurements on an absolute scale from Ref. 31 at $T = 54$ mK ($T = 75$ mK) [red crosses (black dots)], and the computation for $J' = 27$ mK [blue line]. Recent ND measurements as a function of temperature suggest that the data of Ref. 31 was taken at temperatures ∼10 mK higher than the nominal indicated temperature.

A. Zero-temperature correlations and excitations

In a ladder system different types of correlations are possible. We focus here on the quantities

$$S_{q_y}^{\alpha\beta}(q,\omega) = \sum_l \int_{-\infty}^{\infty} dt \langle S_{l,q_y}^{\alpha}(t) S_{0,q_y}^{\beta}\rangle e^{i(\omega t - ql)}, \tag{31}$$

where $S_{l,q_y}^{\alpha} = S_{l,1}^{\alpha} \pm S_{l,2}^{\alpha}$ are the symmetric (+) and antisymmetric (−) operators with a rung momentum $q_y = 0,\pi$ and parity $P = +1,-1$ respectively, $\alpha,\beta = z,+,-$, $S_{l,q_y}^{\alpha}(t) = e^{iHt} S_{l,q_y}^{\alpha} e^{-iHt}$ [for a single ladder H corresponds to the Hamiltonian (2)], and the momentum q is given in reciprocal lattice units a^{-1}. The rung momentum q_y is a good quantum number. The dynamical correlations are directly related to INS measurements (see Sec. VI C). They select different types of rung excitations (as summarized in Table I). Using the reflection and translation invariance of an infinite-size system ($L \to \infty$), we can rewrite the considered correlations (31) in a more explicit form (at zero temperature) (for the considered correlations $S^{\alpha\dagger} = S^{\beta}$), i.e.,

TABLE I. Rung excitations created by the symmetric and antisymmetric operators in the decoupled bond limit. P is the parity of the operators in the rung direction and ΔM^z is the change of the total magnetization.

	S_0^z	S_π^z	S_0^+	S_π^+	S_0^-	S_π^-
$\lvert s\rangle$	0	$\lvert t^0\rangle$	0	$-\sqrt{2}\lvert t^+\rangle$	0	$\sqrt{2}\lvert t^-\rangle$
$\lvert t^+\rangle$	$\lvert t^+\rangle$	0	0	0	$\sqrt{2}\lvert t^0\rangle$	$-\sqrt{2}\lvert s\rangle$
$\lvert t^0\rangle$	0	$\lvert s\rangle$	$\sqrt{2}\lvert t^+\rangle$	0	$\sqrt{2}\lvert t^-\rangle$	0
$\lvert t^-\rangle$	$-\lvert t^-\rangle$	0	$\sqrt{2}\lvert t^0\rangle$	$\sqrt{2}\lvert s\rangle$	0	0
P	+1	−1	+1	−1	+1	−1
ΔM^z	0	0	+1	+1	−1	−1

$$S_{q_y}^{\alpha\beta}(q,\omega) = \frac{2\pi}{L}\sum_{\lambda} \left|\langle\lambda|S_{q_y}^{\beta}(q)|0\rangle\right|^2 \delta(\omega + E_0 - E_\lambda), \tag{32}$$

where $|0\rangle$ denotes the ground state of H with energy E_0, $S_{q_y}^{\beta}(q) = \sum_l e^{-iql} S_{l,q_y}^{\beta}$ and $\sum_\lambda$ is the sum over all eigenstates $|\lambda\rangle$ of H with energy E_λ. The form of Eq. (32) clearly shows that $S_{q_y}^{\alpha\beta}(q,\omega)$ is nonzero if the operator $S_{q_y}^{\beta}$ can create an excitation $|\lambda\rangle$ of energy $E_0 + \omega$ and momentum q from the ground state. The correlations $S_{q_y}^{\alpha\beta}$ are then direct probes of the excitations $|\lambda\rangle$ in the system.

Since the experimentally relevant case (compound BPCB) corresponds to a relatively strong coupling situation [$\gamma \ll 1$, Eq. (8)], we use the decoupled bond limit introduced in Sec. II C to present the expected excitations $|t^+\rangle$, $|t^0\rangle$, $|t^-\rangle$, or $|s\rangle$. In Table I, we summarize the rung excitations created by all the operators $S_{q_y}^{\beta}$ and their properties. For example, the rung parity P is changed by applying an operator with rung momentum $q_y = \pi$ and the z magnetization is modified by $\Delta M^z = \pm 1$ by applying the operators $S_{q_y}^{\pm}$, respectively.

B. Excitations in the spin liquid

Using the decoupled bond limit in the spin liquid phase, the excitations in the system can be pictured as the excitation of rung singlets to rung triplets. At zero magnetic field $h^z = 0$, the system is spin rotational symmetric and the different triplet excitations have the same energy $\sim J_\perp$. It has been seen previously that in this system both single-triplet excitations and two-triplet excitations play an important role.[12–16] We discuss these excitations in the following, focusing on the ones that can be created by the symmetric $S_0^{\alpha\alpha} = 2S_0^{\pm\mp}$ and the antisymmetric $S_\pi^{\alpha\alpha} = 2S_\pi^{\pm\mp}$ correlations (see Fig. 11) for the BPCB parameters (39). Note that these correlations are independent of the direction $\alpha = x,y,z$ due to the spin rotation symmetry. Our results are in very good agreement to previous findings.[13–16]

1. *Single-triplet excitations*

At $h^z = 0$, the system is in a global spin singlet state[1] ($S = 0$). The $q_y = \pi$ correlation couples then to states with an odd number of triplet excitations with rung parity $P = -1$ and total spin $S = 1$, $M^z = \pm 1,0$ (see Table I). Nevertheless, only single-triplet excitations are numerically resolved. Their

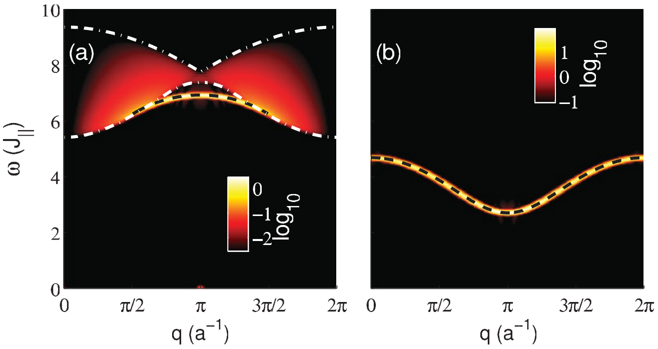

FIG. 11. (Color online) Momentum-energy-dependent correlation functions at $h^z = 0$. (a) Symmetric part $S_0^{\alpha\alpha}(q,\omega)$ with $\alpha = x,y,z$. The dashed (black) line marks the (q,ω) position of the two-triplet bound state [Eq. (61b) in Ref. 14]. The dashed-dotted (white) lines correspond to the boundaries of the two-triplet continuum. (b) Antisymmetric part $S_\pi^{\alpha\alpha}(q,\omega)$. The dashed (black) line corresponds to the predicted dispersion relation of a single-triplet excitation [Eq. (8) in Ref. 13].

spectral weight is concentrated in a very sharp peak, whose dispersion relation can be approximated using a *strong coupling expansion* in γ. Up to first order it is simply given by a cosine dispersion,[12] i.e., $\omega_t(q)/J_\perp \approx 1 + \gamma \cos q$. Further corrections up to third order in γ have been determined in Ref. 13. In Fig. 11(b) we compare the numerical results for the BPCB parameters (39) to the expression up to third order in γ. The strong coupling expansion describes very well the position of the numerically found excitations.

2. *Two-triplet excitations*

The structure of the $q_y = 0$ correlation is more complex [Fig. 11(a)]. Due to the rung parity $P = 1$ of the operators S_0^α, the excitations correspond to an even number of triplet excitations with total spin $S = 1$, $M^z = \pm 1, 0$. We focus here on the two-triplet excitations that can be resolved numerically. These can be divided into a broad continuum and a very sharp triplet ($S = 1$) bound state of a pair of rung triplets. Since these excitations stem from the coupling to triplets already present in the ground state (Fig. 4), their amplitude for the considered BPCB parameters (39) is considerably smaller than the weight of the single-triplet excitations.[16]

The dispersion relation of the bound states has been calculated using a linked cluster series expansion.[14] The first terms of the expansion have an inverse cosine form and the bound state only exists in an interval at approximately $q = \pi$ (cf. Refs. 14 and 15). The numerical results for the BPCB parameters (39) agree very well with the analytic form of the dispersion [Fig. 11(a)]. The upper and lower limits of the continuum can be determined by considering the boundary of the continuum formed by two noninteracting triplets. They are numerically computed using the single-triplet dispersion [Eq. (8) in Ref. 13] shown in Fig. 11(a). They agree very well with the numerically found results. The comparison with the known solutions serves as a check of the quality of our numerical results.

C. Excitations in the gapless regime

A small applied magnetic field ($h^z < h_{c1}$), at first order, only smoothly translates the excitations shown in Fig. 11 by an energy $-h^z M^z$ due to the Zeeman effect. However, if the magnetic field exceeds h_{c1}, the system enters into the gapless regime with a continuum of excitations at low energy. For small values of γ most features of this low-energy continuum are qualitatively well described by considering the lowest two modes of the ladder only. Beside the low-energy continuum, a complex structure of high-energy excitations exist. Contrarily to the low-energy sector, this structure crucially depends on the high-energy triplet modes. In the following, we give a simple picture for these excitations starting from the decoupled bond limit.

1. *Characterization of the excitations in the decoupled bond limit*

The evolution of the spectra for the BPCB parameters with increasing magnetic field are presented in Fig. 12 for $S_{q_y}^{zz}$, in Fig. 13 for $S_{q_y}^{+-}$, and in Fig. 14 for $S_{q_y}^{-+}$. Three different classes of excitations occur: (i) a continuum of excitations at low energy for S_0^{zz} and $S_\pi^{\pm\mp}$; (ii) single-triplet excitations at higher energy with a clear substructure for S_π^{zz}, S_0^{+-}, and S_π^{+-}; and (iii) excitations at higher energy for S_0^{zz} and S_0^{+-} and S_0^{-+} stemming from two-triplet excitations that have their main weight at approximately $q \approx \pi$.

In the following we summarize some of the characteristic features of these excitations, before we study them in more detail in Secs. V C 2–V C 3 b.

(i) The continuum at low energy that does not exist in the spin liquid is a characteristic signature of the gapless regime. It stems from excitations within the low-energy band that corresponds to the $|s\rangle$ and $|t_+\rangle$ states in the decoupled bond limit [cf. Fig. 2(a) and Table I]:

S_0^{zz}: excitations within the triplet $|t_+\rangle$ mode;
$S_\pi^{\mp\pm}$: excitations between the singlet $|s\rangle$ and the triplet $|t_+\rangle$ mode.

This continuum is smoothly connected to the spin liquid spectrum in the case of S_π^{-+}. It originates from the single-triplet $|t^+\rangle$ branch (Sec. V B 1) when the latter reaches the ground-state energy due to the Zeeman effect. Since two modes play the main role in the description of these low-energy features, many of them already can be explained qualitatively by the spin chain mapping. The excitations in the chain have been studied previously by using a BA description and exact diagonalization calculations in Ref. 73. More recently they were computed in Ref. 35 due to recent progress in the BA method. In particular, the boundary of the spectrum at low energy is well described by this approach, because the LL velocity determining it is hardly influenced by the higher modes (cf. Fig. 23). However, a more quantitative description requires to take into account the higher modes of the system as well. In Sec. V C 2 we compare in detail our results with the LL theory and the spin chain mapping, pointing out their corresponding ranges of validity.

(ii) The single high-energy triplet excitations form a continuum with a clear substructure. In the decoupled bond limit, these excitations correspond to the following:

S_π^{zz}: single-triplet excitations $|t^0\rangle$ at energy $\sim h^z$;
S_0^{+-}: single-triplet excitations $|t^0\rangle$ at energy $\sim h^z$;
S_π^{+-}: single-triplet excitations $|t^-\rangle$ at energy $\sim 2h^z$.

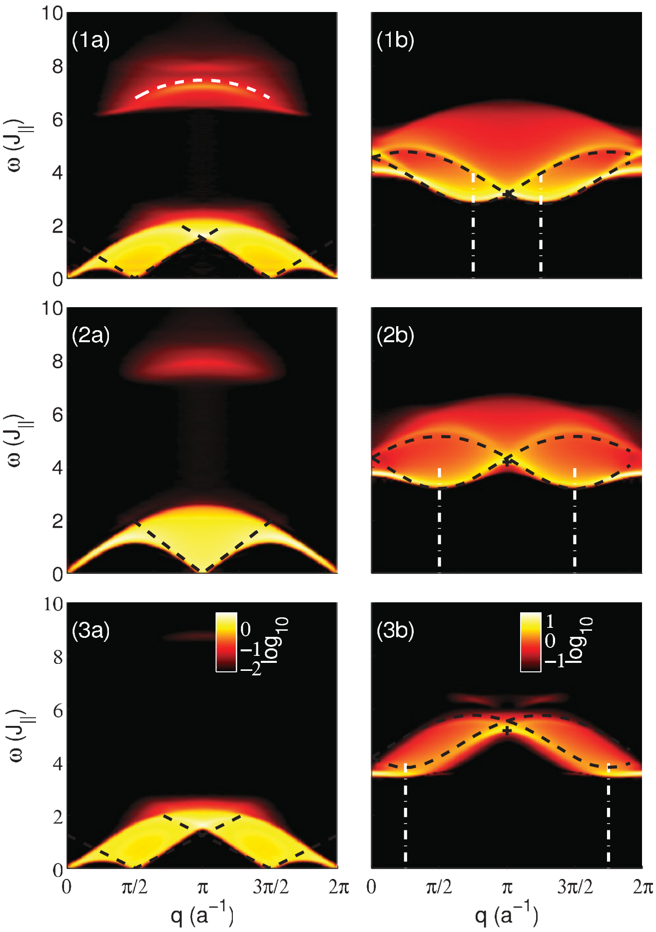

FIG. 12. (Color online) Momentum-energy-dependent *zz*-correlation function (1) at $m^z = 0.25$ ($h^z = 3.153J_\parallel$), (2) at $m^z = 0.5$ ($h^z = 4.194J_\parallel$), and (3) at $m^z = 0.75$ ($h^z = 5.192J_\parallel$). (a) Symmetric part $S_0^{zz}(q,\omega)$ without Bragg peak at $q = 0$. The dashed black lines correspond to the location of the slow divergence at the lower edge of the continuum predicted by the LL theory. The dashed white curve corresponds to the predicted two-triplet bound-state location. (b) Antisymmetric part $S_\pi^{zz}(q,\omega)$. The dashed black lines correspond to the position of the high-energy divergences or cusps predicted by the approximate mapping on the *t*-*J* model. The vertical white dashed-dotted lines mark the momenta of the minimum energy of the high-energy continuum and the black cross is the energy of its lower edge (Ref. 20) at $q = \pi$.

Many of the features of these continua can be understood by mapping the problem onto a mobile hole in a chain, as pointed out first in Ref. 74. We detail this mapping in Sec. V C 3 and Appendix A. It opens the possibility to investigate the behavior of a single hole in a *t*-*J*-like model by using experiments in pure spin ladder compounds.

(iii) The high-energy continuum, which has almost no weight close to the Brillouin zone boundary ($q = 0,2\pi$), is related to two-triplet excitations of the spin liquid (Sec. V B 2). They are generated from high-energy triplet components of the ground state. Their weight therefore vanishes for $\gamma \to 0$ and the excitations correspond to the following:

S_0^{-+}: two-triplet excitations. $\frac{1}{\sqrt{2}}(|t^0\rangle|t^+\rangle - |t^+\rangle|t^0\rangle)$ at energy $\sim h^z$;

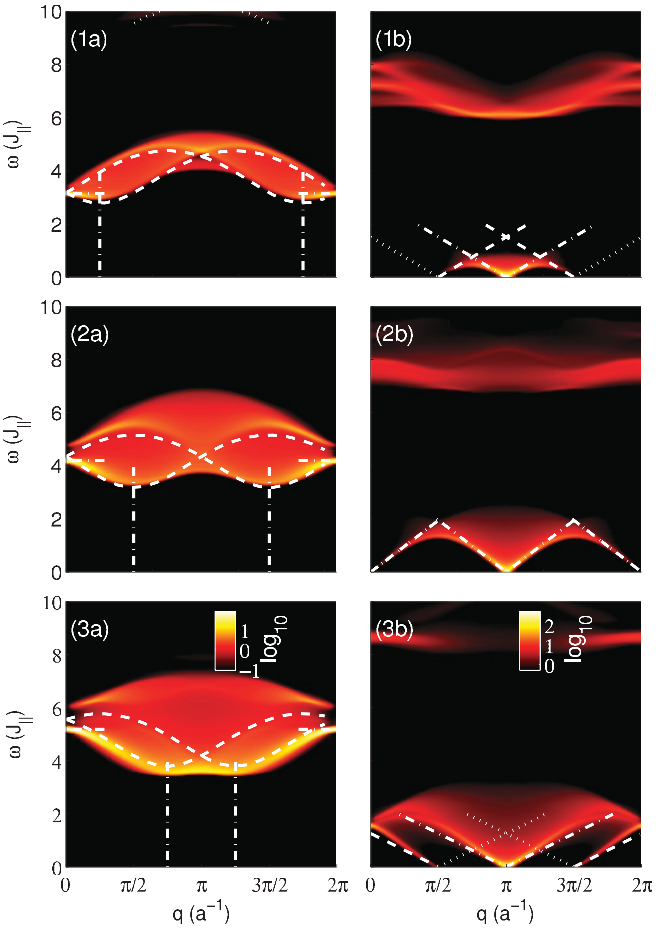

FIG. 13. (Color online) Momentum-energy-dependent +− correlation function (1) at $m^z = 0.25$ ($h^z = 3.153J_\parallel$), (2) at $m^z = 0.5$ ($h^z = 4.194J_\parallel$), and (3) at $m^z = 0.75$ ($h^z = 5.192J_\parallel$). (a) Symmetric part $S_0^{+-}(q,\omega)$. The vertical dashed-dotted white lines mark the momenta of the minimum energy of the high energy continuum and the horizontal ones the frequency of its lower edge (Ref. 20) at $q = 0, 2\pi$. The dashed white lines correspond to the position of the high energy divergences or cusps predicted by the approximate mapping on the *t*-*J* model. The dotted white curve corresponds to the predicted two-triplet bound-state location. The high-energy excitations at $\omega = 3h_z$ are hardly visible. (b) Antisymmetric part $S_\pi^{+-}(q,\omega)$. The dashed and dashed-dotted (dotted) white lines correspond to the location of the strong divergence (cusp) at the lower edge of the continuum predicted by the LL theory.

S_0^{zz}: two-triplet excitations $\frac{1}{\sqrt{2}}(|t^+\rangle|t^-\rangle - |t^-\rangle|t^+\rangle)$ at energy $\sim 2h^z$;

S_0^{+-}: two-triplet excitations $\frac{1}{\sqrt{2}}(|t^0\rangle|t^-\rangle - |t^-\rangle|t^0\rangle)$ at energy $\sim 3h^z$.

2. *Low-energy continuum*

In this section we concentrate on the low-energy excitations of type (i), discussing first their support and then comparing their spectral weight to the LL prediction.

a. Support of the low-energy excitations. The position of the soft modes in the low-energy continuum can be directly obtained from the bosonization representation[2,19,20] (see Appendix B 2). They can also be understood in a simple

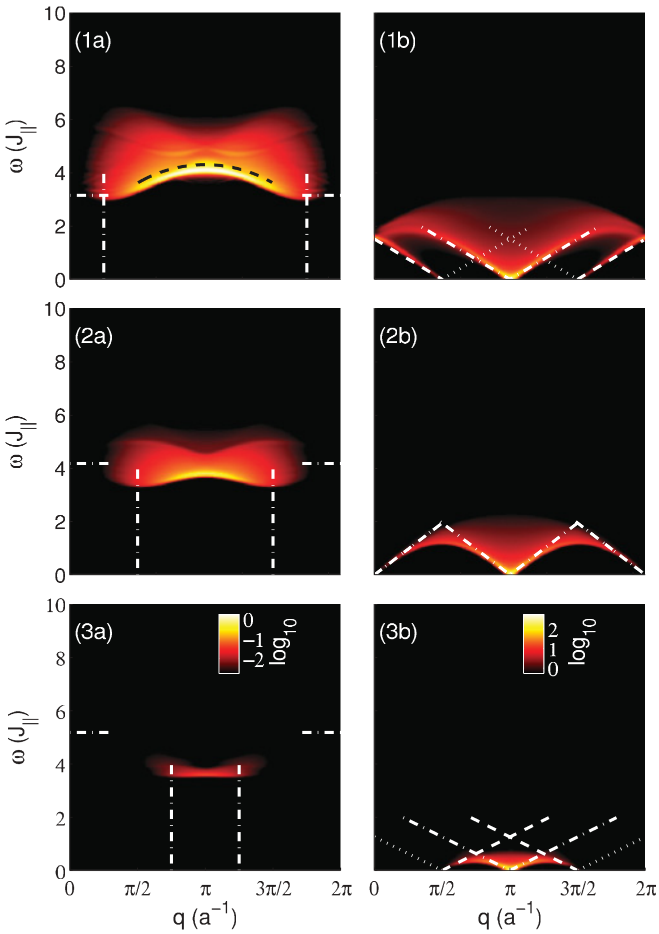

FIG. 14. (Color online) Momentum-energy-dependent $-+$ correlation function (1) at $m^z = 0.25$ ($h^z = 3.153 J_\parallel$), (2) at $m^z = 0.5$ ($h^z = 4.194 J_\parallel$), and (3) at $m^z = 0.75$ ($h^z = 5.192 J_\parallel$). (a) Symmetric part $S_0^{-+}(q,\omega)$. The vertical dashed-dotted white lines correspond to the momenta at which the minimum energy of the high energy continuum occurs and the horizontal line to the frequency of its lower edge (Ref. 20) at $q = 0, 2\pi$. The dashed black curve corresponds to the predicted two-triplet bound-state location. (b) Antisymmetric part $S_\pi^{-+}(q,\omega)$. The dashed and dashed-dotted (dotted) white lines correspond to the location of the strong divergence (cusp) at the lower edge of the continuum predicted by the LL theory.

picture that we outline in the following. The distribution of the rung state population in the ground state depends on the magnetic field h^z (see Fig. 4). Taking a fermionic point of view, the magnetic field acts as a chemical potential that fixes the occupation of the singlet and triplet rung states. Increasing the magnetic field reduces the number of singlets, whereas at the same time the number of triplets increases (see the sketch in Fig. 15). The Fermi level lies at the momenta $q = \pi m^z, \pi(2 - m^z)$ for the singlet states and at the momenta $q = \pi(1 - m^z), \pi(1 + m^z)$ for the triplet states. In this picture the soft modes correspond to excitations at the Fermi levels. For transitions $|t^+\rangle \leftrightarrow |t^+\rangle$ the transferred momenta of these zero-energy excitations are $q = 0, 2\pi m^z, 2\pi(1 - m^z)$. In contrast, the interspecies transitions $|t^+\rangle \leftrightarrow |s\rangle$ allow the transfer of $q = \pi(1 - 2m^z), \pi, \pi(1 + 2m^z)$. Therefore the positions of the soft modes in the longitudinal correlation S_0^{zz}, which allows transitions within the triplet states, shift from the boundaries of the Brillouin zone inward toward $q = \pi$ when m^z increases [Fig. 12(a)]. In contrast, the positions of the soft modes in the transverse correlations $S_\pi^{\pm\mp}$, which allow transitions between the singlets and the triplets, move with increasing magnetic field outward [Figs. 13(b) and 14(b)].

The top of these low-energy continua are reached when the excitations reach the boundaries of the energy band. In particular, the maximum of the higher boundary lies at the momentum $q = \pi$, which is easily understood within the simple picture drawn above (cf. Fig. 15). A more detailed description of different parts of these low-energy continua is given in Ref. 73.

Let us compare the above findings with the predictions of the LL theory for the dynamical correlations.[2,19,20] Details on the LL description of the correlations are given in Appendix B 2. The LL theory predicts a linear momentum-frequency dependence of the lower continuum edges with a slope given by the LL velocity $\pm u$ (Fig. 23). The position of the soft modes are given by the ones outlined above (see Fig. 24). The predicted support at low energy agrees very well with the numerical results [Figs. 12(a), 13(b), and 14(b)]. Of course, when one reaches energies of order $J_\parallel$ in the spectra, one cannot rely on the LL theory anymore. This is true in particular for the upper limit of the spectra.

b. Spectral weight of the excitations. Let us now focus on the distribution of the spectral weight in the low-energy continuum. In particular, we compare our numerical findings to the LL description. Qualitatively, the LL theory predictions for the low-energy spectra are well reproduced by the DMRG computations.

The LL predicts typically an algebraic behavior of the correlations at the low-energy boundaries that can be a divergence or a cusp.

S_0^{zz}: The LL predicts peaks at the $q = 0, 2\pi$ branches and a slow divergence at the lower edge of the incommensurate branches $q = 2\pi m^z, 2\pi(1 - m^z)$ (with exponent $1 - K \approx 0.2 \ll 1$). In the numerical results [Fig. 12(a)] a slight increase of the weight toward the lower edge of the incommensurate branches can be seen.

S_π^{+-}: A strong divergence at the lower edge of the $q = \pi$ branch (with exponent $1 - 1/4K \approx 3/4 \gg 0$) is obtained within the LL description. This is in good qualitative agreement with the strong increase of the spectral weight observed in the numerical data. A more interesting behavior is found close to the momenta $q = \pi(1 \pm 2m^z)$ in the incommensurate branches. Here a strong divergence is predicted for momenta higher (lower) than the soft mode $q = \pi(1 - 2m^z)$ [$q = \pi(1 + 2m^z)$] with exponent $1 - \eta_- \approx 3/4 \gg 0$. In contrast, for momenta lower (higher) than the soft mode

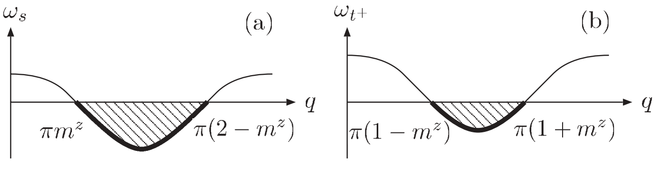

FIG. 15. Fermionic picture for the effect of the magnetic field. Filling of (a) the singlet band $|s\rangle$ and (b) the triplet band $|t^+\rangle$ in the gapless phase for a given magnetization m^z.

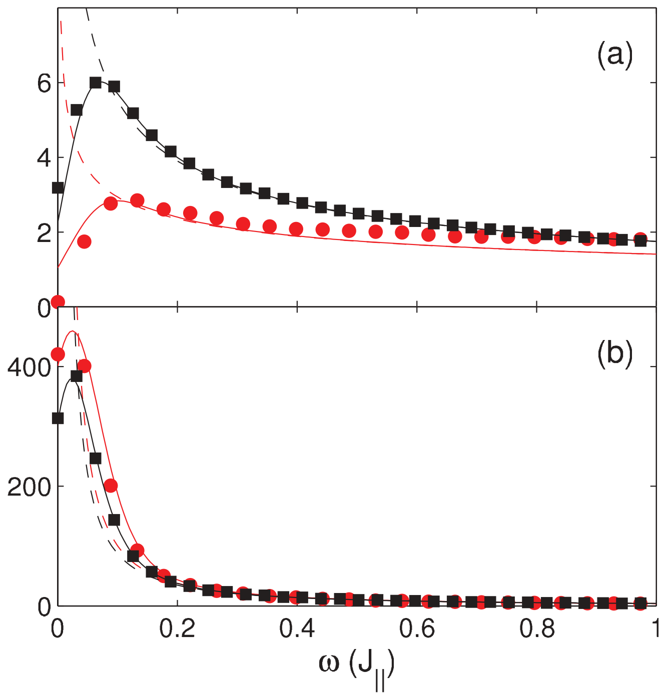

FIG. 16. (Color online) Cuts at fixed momentum $q = \pi$ and magnetization $m^z = 0.5$ of the low-energy spectrum (a) $S_0^{zz}(q = \pi,\omega)$ and (b) $S_\pi^{-+}(q = \pi,\omega)$. The (red) circles and the (black) squares are the numerical results for the ladder and its spin chain mapping, respectively. The dashed lines correspond to the LL predictions, and the solid lines are the latter convolved with the same Gaussian filter than the numerical data. The DMRG frequency numerical limitation is of the order of the peak broadening of width $\delta\omega \approx 0.1 J_\parallel$ (see Appendix C 3).

$q = \pi(1 - 2m^z)$ [$q = \pi(1 + 2m^z)$], a cusp with exponent $1 - \eta_+ \approx -5/4 \ll 0$ is expected.[75] In the numerical results [Fig. 13(b)] this very different behavior below and above the soft modes is evident. The divergence and cusp correspond to a large and invisible weight, respectively.

S_π^{-+}: The same behavior as S_π^{+-} replacing $m^z \to -m^z$ can be observed in Fig. 14(b).

To compare quantitatively the predictions of the LL to the numerical results, in Fig. 16 we show different cuts of the correlations at fixed momentum $q = \pi$ and magnetization $m^z = 0.5$ for the ladder and the spin chain mapping. These plots show the DMRG results, the LL description, and the latter convolved with the Gaussian filter. The filter had been used in the numerical data to avoid effects due to the simulated finite-time interval (see Appendix C 3). Note that the amplitude of the LL results are inferred from the static correlation functions, such that the LL curve is fully determined and *no fitting parameter* is left. Therefore, the convolved LL results can directly be compared to the numerical results. Even though the presented numerical resolution might not be good enough to resolve the behavior close to the divergences (cusps), interesting information such as the arising differences between the spin chain mapping and the full ladder calculations already can be extracted. In Fig. 16(a), we show a cut through the correlation at fixed momentum $S_0^{zz}(q = \pi,\omega)$. The convolved LL and the numerical results compare very well. The difference between the real ladder calculations and the spin chain mapping that neglect the effects of the higher triplet states $|t^-\rangle$, $|t^0\rangle$ is obvious. From the LL description point of view, the shift of the spin chain correlation compared to the real ladder curve comes mainly from the prefactor A_z and the algebraic exponent, which are clearly modified by the effects of the high-energy triplets (see Fig. 23).

For the transverse correlations, the LL theory predicts a strong divergence (with an exponent $1 - 1/4K \approx 3/4 \gg 0$) at the lower boundary of the continuum branch at $q = \pi$. A cut through the low-energy continuum $S_\pi^{-+}(q = \pi,\omega)$ is shown in Fig. 16(b). The convolved LL reproduces well the numerical results.

3. *High-energy excitations*

a. Weak coupling description of the high-energy excitations. Before looking in detail at the two kinds of high-energy excitations presented in Sec. V C 1, we compare our computed high-energy spectra with the weak coupling description ($\gamma \gg 1$). In this limit information on the spectrum can be extracted from the bosonization description.[2,19,20] In particular, one expects a power-law singularity at the lower edge continuum with a minimal position at $q = \pi(1 \pm m^z)$ (for S_π^{zz}), $q = \pi m^z, \pi(2 - m^z)$ (for $S_0^{\pm\mp}$), and an energy h^z at momentum $q = \pi$ (for S_π^{zz}), $q = 0$ (for $S_0^{\pm\mp}$). Except for S_0^{-+}, in which the spectral weight is too low for a good visualization, our computed spectra reproduces well the predictions for the minimal positions, even though the coupling strength considered is not in the weak coupling limit [cf. Figs. 12(b), 13(a), and 14(a)].

b. High-energy single-triplet excitations. The high-energy single-triplet continua originate from the transition of the low-energy rung states $|s\rangle$ and $|t^+\rangle$ to the high-energy triplets $|t^0\rangle$ and $|t^-\rangle$. The excitations coming from the singlets $|s\rangle$ (in S_π^{zz} and S_π^{+-}) are already present in the spin liquid phase (cf. Sec. V B 1) in which they have the shape of a sharp peak centered on the triplet dispersion. The transition between the gapped spin liquid and the gapless regime is smooth and consists of a splitting and a broadening of the triplet branch that generates a broad continuum of new excitations. Contrarily to the latter, the excitations coming from the low-energy triplets $|t^+\rangle$ (in S_0^{+-}) are not present in the spin liquid phase. The corresponding spectral weight appears when $h^z > h_{c1}$.

An interpretation of the complex structure of these high-energy continua can be obtained in terms of itinerant quantum chains. Using a strong coupling expansion of the Hamiltonian (2) (Appendix A), it is possible to map the high-energy single-triplet excitations $|t^0\rangle$ to a single hole in a system populated by two types of particles with pseudospin $|\tilde{\uparrow}\rangle = |t^+\rangle$, $|\tilde{\downarrow}\rangle = |s\rangle$ (with the Sec. II C notation).

In this picture the effective Hamiltonian of the $J_\perp$ energy sector is approximately equivalent to the half-filled anisotropic 1D *t*-*J* model with one hole (see Appendix A 3 b). The effective Hamiltonian is given by

$$H_{t\text{-}J} = H_{XXZ} + H_t + H_{\text{s-h}} + \epsilon, \qquad (33)$$

where $\epsilon = (J_\perp + h^z)/2$ is an energy shift and $H_t = J_\parallel/2 \sum_{l,\sigma}(c_{l,\sigma}^\dagger c_{l+1,\sigma} + \text{h.c.})$ is the usual hopping term. Here $c_{l,\sigma}^\dagger$ ($c_{l,\sigma}$) is the creation (annihilation) operator of a fermion with pseudospin $\sigma = \tilde{\uparrow}, \tilde{\downarrow}$ at the site l. Note that although we are dealing here with spin states, it is possible to faithfully represent the three states of each site's Hilbert space ($|s\rangle$, $|t^+\rangle$, $|t^0\rangle$) by using a fermion representation.

Additionally to the usual terms of the *t*-*J* model, a nearest-neighbor interaction term between one of the spins and the hole arises:

$$H_{\text{s-h}} = -\frac{J_\parallel}{4}\sum_l [n_{l,\text{h}} n_{l+1,\tilde{\uparrow}} + n_{l,\tilde{\uparrow}} n_{l+1,\text{h}}]. \tag{34}$$

Here $n_{l,\text{h}}$ is the density operator of the hole on the site l. In this language the spectral weight of S^{zz}_π and S^{+-}_0 corresponding to the single high-energy triplet excitations is equivalent to the single-particle spectral functions of the up-spin and down-spin particle, respectively:

$$\begin{aligned} S^{zz}_\pi &\propto \langle c^\dagger_{\tilde{\downarrow}} c_{\tilde{\downarrow}}\rangle \quad \text{with hole of type} \quad |s\rangle \to |t^0\rangle, \\ S^{+-}_0 &\propto \langle c^\dagger_{\tilde{\uparrow}} c_{\tilde{\uparrow}}\rangle \quad \text{with hole of type} \quad |t^+\rangle \to |t^0\rangle. \end{aligned} \tag{35}$$

Here $\langle c^\dagger_\sigma c_\sigma\rangle(q,\omega) = \sum_\lambda |\langle\lambda|c_{q,\sigma}|0\rangle|^2\delta(\omega + E_0 - E_\lambda)$.

For the standard *t*-*J* model [for SU(2)-invariant *XXX* spin background and without the anisotropic term $H_{\text{s-h}}$ in Eq. (33)], these spectral functions have been studied in Refs. 76 and 77. The presence of singularities of the form

$$\langle c^\dagger_\sigma c_\sigma\rangle(q,\omega) \propto [\omega - \omega_{t^0}(q - q_\nu)]^{2X_\nu(q)-1} \tag{36}$$

were found. Here $\omega_{t^0}(q)$ is the $|t^0\rangle$ triplet dispersion relation, q_ν is the spinon momentum at the Fermi level, and X_ν is the algebraic decay exponent at the singularity. This exponent is not known in our case and depends on the magnetization m^z and the momentum q. It generates a peak or a cusp at the energy $\omega = \omega_{t^0}(q - q_\nu)$. The spinon momentum q_ν depends on the type of the rung state before excitation ($\nu = s, t^+$). For an excitation created from a singlet state, $q_s = \pm\pi m^z$ (for S^{zz}_π), and from the triplet state, $q_{t^+} = \pi(1 \pm m^z)$ (for S^{+-}_0) (Fig. 15). At $h^z = 0$, a series expansion of $\omega_{t^0}(q)$ can be performed [Eq. (8) in Ref. 13 and denoted $\omega_t(q)$ in Sec. V B 1]. To extend it into the gapless phase ($h_{c1} < h^z < h_{c2}$), we approximate $\omega_{t^0}(q)$ by shifting the value $\omega_t(q)$ at $h^z = 0$ by the Zeeman shift, i.e.,

$$\omega_{t^0}(q) = \omega_t(q) + \Delta E_0(h^z). \tag{37}$$

Here we used the shift of the ground-state energy per rung $\Delta E_0(h^z) = E_0(h^z) - E_0(0)$. The ΔE_0 was determined by DMRG calculations [Fig. 25(b) for the BPCB parameters]. The resulting momentum-frequency positions $\omega = \omega_{t^0}(q - q_\nu)$ of the high-energy singularities (cusps or divergencies) are plotted on the spectrum [see Figs. 12(b) and 13(a)]. They agree remarkably well with the shape of the computed spectra in particular for a small magnetic field.[78] Neglecting the additional interaction term $H_{\text{s-h}}$ the *t*-*J* model Hamiltonian would lead to a symmetry of these excitations with respect to half magnetization. However, in the numerical spectra the effect of the interaction shows up in a clear asymmetry of these excitations [Figs. 12(1b) and 13(3a)]. In particular, in the S^{+-}_0 correlation, some of the weight is seemingly detaching and pushed toward the upper boundary of the continuum [Fig. 13(3a)] for large magnetization. A more detailed account of the spectra can be found in Ref. 79.

A similar mapping can be performed for the single $|t^-\rangle$ excitation. In contrast to the $J_\perp$ sector, in the $2J_\perp$ sector not only the $|t^-\rangle$ excitation occurs, but the effective Hamiltonian mixes also $|t^0\rangle$ triplets into the description. Therefore, the description by a single hole in a spin-1/2 chain breaks down and more local degrees of freedom are required. This results in a more complex structure as seen in Fig. 13(1b). Previously high-energy excitations in dimerized antiferromagnets have been described rather generally by a mapping to an x-ray edge singularity problem.[80–82] It is interesting though that in the present setup these excitations can be understood as *t*-*J* hole spectral functions, which display a much richer structure than anticipated.

c. High-energy two-triplet excitations. The two-triplet continua and bound states already discussed in the spin liquid phase (cf. Sec. V B 2) are still visible in the gapless regime in the symmetric correlations (S^{zz}_0 and $S^{\pm\mp}_0$). At low magnetic field the location of their maximal spectral weight can be approximated by the expression of the bound-state dispersion at zero field [Eq. (61b) in Ref. 14] shifted by the Zeeman energy (the Zeeman shift includes both the shift of the ground state [Fig. 25(b)] and the shift of the excited state). The two-triplet excitation location obtained in this way agrees to a good extent with the location found in the numerical calculations [cf. Figs. 12(1a), 13(1a), and 14(1a)]. Since these excitations are generated from the high-energy triplet components in the ground state and these vanish with increasing magnetic field (cf. Fig. 4), their residual spectral weight slowly disappears with increasing magnetization.

D. Weak-to-strong coupling evolution

For all the excitation spectra presented above, the intrachain coupling ratio of BPCB $\gamma = J_\parallel/J_\perp \approx 1/3.55 \ll 1$ was taken. For this chosen value of γ, a strong coupling approach gives a reasonable description of the physics. In this section we discuss the evolution of the spectra from weak ($\gamma \to \infty$) to strong coupling ($\gamma \to 0$). To illustrate this behavior, we show in Fig. 17 the symmetric and antisymmetric parts of the correlations $S^{+-}_{q_y}$ at $m^z = 0.25$ for different coupling ratios $\gamma = \infty, 2, 1, 0.5, 0$.

At $\gamma \to \infty$ [Fig. 17(1)], the chains forming the ladder correspond to two decoupled Heisenberg chains. In this case the symmetric and antisymmetric correlations are identical, $S^{+-}_0 = S^{+-}_\pi$, and are equivalent to the correlation $2S^{+-}$ of the single chain[73] with magnetization per spin $m^z/2 = 0.125$. A complex low-energy continuum exists with zero-energy branches[6,19,73] at momenta $q = \pm\pi m^z, \pi$, similar to that discussed in Sec. V C 2. In contrast, in the strong coupling limit ($\gamma \to 0$) [Fig. 17(5b)] the symmetric correlations vanish and the antisymmetric part corresponds to the single chain correlation $2S^{+-}$ with anisotropy $\Delta = 1/2$ and magnetization per spin $m^z - 1/2$ (see the spin chain mapping in Sec. II C). The antisymmetric part consists of a low-energy continuum with branches at momenta $q = (1 \pm 2m^z)\pi, \pi$ (Sec. V C 2). Note that a bosonization description of the low-energy sectors of both extreme regimes can be formulated[2,19,20] (see Appendix B2).

In the following we discuss the evolution between these two limits. In the antisymmetric correlation [cf. Figs. 17(2)–17(5b)] a low-energy continuum exists at all couplings with a zero-energy excitation branch at $q = \pi$. These low-energy

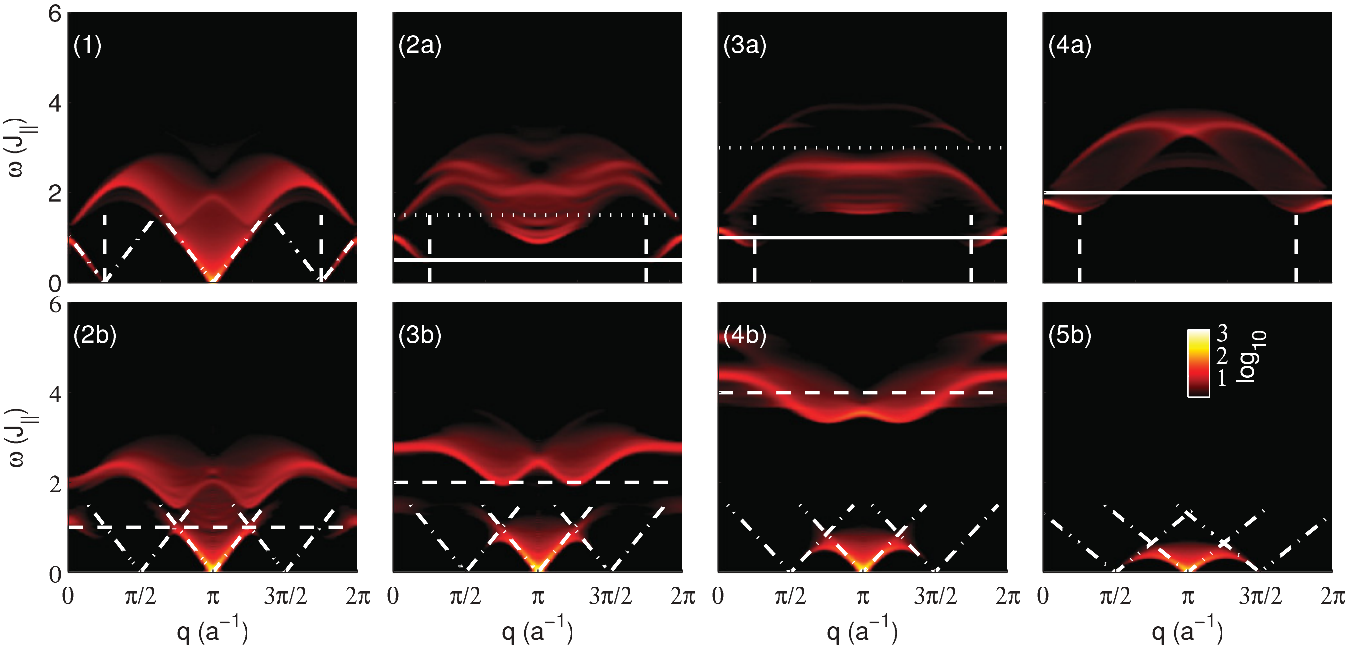

FIG. 17. (Color online) Momentum-energy-dependent +− correlations [$S^{+-}_{q_y}(q,\omega)$] at $m^z = 0.25$ for different ladder couplings ($\gamma = J_\parallel/J_\perp$): (1) $\gamma \to \infty$, (2) $\gamma = 2$, (3) $\gamma = 1$, (4) $\gamma = 0.5$, (5) $\gamma \to 0$. The symmetric (antisymmetric) correlations with $q_y = 0$ ($q_y = \pi$) are presented in the figures labeled by a (b). In (1), (2a)–(4a) the vertical dashed lines represent the incommensurate momenta of the low-energy branches of the single spin chain at $q = \pm\pi m^z = \pm\pi/4$ [they also correspond to the predicted momenta of the lowest-energy excitations of the symmetric correlations (Ref. [20])]. The horizontal solid (dotted) horizontal lines in (2a)–(4a) correspond to the approximate energy $J_\perp$ ($3J_\perp$) of the single-triplet excitations of type (ii) (two-triplet excitations of type (iii)). The horizontal dashed lines in (2b)–(4b) correspond to the approximate energy $2J_\perp$ of the excitations of type (ii). The dashed-dotted lines in (1) correspond to the linear low-energy boundaries of the continuum of excitations given by the LL theory applied on single Heisenberg chains $\gamma \to \infty$. The dashed-dotted lines in (2b)–(5b) correspond to the linear low-energy boundaries of the continuum of excitations given by the LL theory on spin ladder with finite γ (see Appendix B 2).

excitations correspond mainly to the excitations with $\Delta S = \Delta M^z = -1$. This has been pointed out for the weak coupling limit.[19,73] They become the transitions $|t^+\rangle \to |s\rangle$ with the same quantum numbers in the decoupled bond limit. Additionally, the upper part of the excitation spectrum at weak coupling, which corresponds mainly to excitations with[73] $\Delta S = 0, 1$ and $\Delta M^z = -1$, splits from the lower part of the spectrum and moves to higher energy while increasing the coupling. It evolves to a high-energy excitation branch, which corresponds in the decoupled bond limit to the $|s\rangle \to |t^-\rangle$ transition, i.e., single-triplet excitations of type (ii) (see Sec. V C 3 b) at $\sim 2J_\perp$.[83]

The properties of the zero-energy excitation branch at $q = \pi$ show a smooth transition between the two limits.[2,19] For example, the slope of the lower edge continuum, which is determined by the LL velocity u, decreases smoothly from its value for the Heisenberg chain to the lower value for the anisotropic spin chain with $\Delta = 1/2$ in the strong coupling limit. In contrast to this smooth change, the presence of a finite value of $J_\perp$ leads to the formation of a gap in the incommensurate low-energy branches[19] at $q = \pm\pi m^z$. With increasing coupling strength $J_\perp$, new low-energy branches at momenta $q = \pi(1 \pm 2m^z)$ become visible.[2,20] The weight of these gapless branches is very small for small coupling and increases with stronger coupling.[2]

In contrast to the antisymmetric part, the symmetric part S_0^{+-} becomes gapped when the interladder coupling $J_\perp$ is turned on. The lowest-energy excitations remain close to the momenta $q = \pm\pi m^z$, in agreement with Ref. [20]. They connect to the single-triplet excitations of type (ii) (see Sec. V C 3 b), which are approximately at an energy $J_\perp$. During increasing γ, the higher part of the spectrum starts to separate from the main part and evolves to a branch of high-energy two-triplet excitations of type (iii) (see Sec. V C 3 c). These are located at $\sim 3J_\perp$. Our computed spectra for $\gamma = 2,1,0.5$ presented in Figs. 17(2a)–17(4a) clearly show this behavior. In Fig. 17(4a) the highest two-triplet excitations cannot be seen anymore because their spectral weight is too low.

E. Influence of the weak interladder coupling on the excitation spectrum

Up to now we only discussed the excitations of a single spin ladder and neglected the weak interladder coupling J' usually present in real compounds.

Deep inside of the spin liquid phase, the correlations for a single ladder are dominated by high-energy single-triplet or multi-triplet excitations, as discussed in Sec. V B. The presence of a small interladder coupling J' causes a dispersion in the interladder direction with an amplitude of order J'. This effect can be evaluated for independent triplet excitations using a single-mode approximation.[1] However, for the compound BPCB, the interladder coupling is so small that present-day experiments do not resolve this small broadening.[32,33]

In contrast, in the gapless phase the effect of the interladder coupling can change considerably the excitations. In particular, below the transition temperature to the 3D-ordered phase, a Bragg peak appears at $q = \pi$ in the transverse dynamical functions $S_{\pi}^{\pm\mp}$. As discussed in Ref. 58, this Bragg peak is surrounded by gapless Goldstone modes, and it has been measured in the compound BPCB.[31] Additional high-energy modes are predicted to occur in the transverse $S_{\pi}^{\pm\mp}$ and longitudinal S_{0}^{zz}.[58] It would be interesting to compute the excitations using a random-phase approximation analogously to Ref. 58, in combination with the computed dynamical correlations for the single ladder, in order to investigate the effect of a weak interladder coupling in more detail. However, this goes beyond the scope of the present work and will be left for a future study.

VI. EXPERIMENTAL MEASUREMENTS

In this section we summarize the results of experiments on the compound BPCB and compare them to the theoretical predictions. First, we introduce the structure of the BCPB compound. Then we focus on static and low-energy results of the system. Finally, we discuss the detection of excitations by INS[32,33] measurements. In particular, we give a prediction of the INS cross section in a full range of energy and compare its low-energy part with the measured spectra on the compound BPCB.

A. Structure of the compound $(C_5H_{12}N)_2CuBr_4$

The compound $(C_5H_{12}N)_2CuBr_4$, customarily called BPCB or $(Hpip)_2CuBr_4$, has been intensively investigated using different experimental methods such as NMR,[30] ND,[31] INS,[32,33] calorimetry,[29] magnetometry,[84] magnetostriction,[85,86] and electron-spin-resonance spectroscopy[87] (ESR).

The magnetic properties of the compound are related to the unpaired highest-energy orbital of the Cu^{2+} ions. Thus the corresponding spin structure (Fig. 18) matches with the Cu^{2+} location.[28,30,32] The unpaired spins form two types of inequivalent ladders (Fig. 18) along the **a** axis (**a**, **b**, and **c** are the unit cell vectors of BPCB). The directions of the rung vectors of these ladders are $\mathbf{d}_{1,2} = (0.3904, \pm 0.1598, 0.4842)$ in the primitive vector coordinates [Fig. 18(b)]. As one can see from the projection of the spin structure onto the **bc** plane [Fig. 18(b)], each rung has $n_c = 4$ interladder neighboring spins.

The BPCB structure has been identified as a good experimental realization of the system of weakly coupled spin-1/2 ladders[28] described by the Hamiltonian (1). As we will explain in the next section, the interladder coupling J' has been experimentally determined to be[30,31]

$$J' \approx 20\text{–}100 \text{ mK}. \tag{38}$$

The intraladder couplings from Eq. (2) were determined to be $J_\perp \approx 12.6$–13.3 K and $J_\parallel \approx 3.3$–3.8 K with different experimental techniques and at different experimental conditions.[28–33,84–86] In this paper, we use the values[88]

$$J_\perp \approx 12.6 \text{ K}, \quad J_\parallel \approx 3.55 \text{ K}. \tag{39}$$

Recently a slight anisotropy of the order of 5% of $J_\perp$ has been discovered by ESR[87] measurements. This anisotropy could explain the small discrepancies between the couplings found in different experiments. The magnetic field in Tesla is related to h^z, replacing

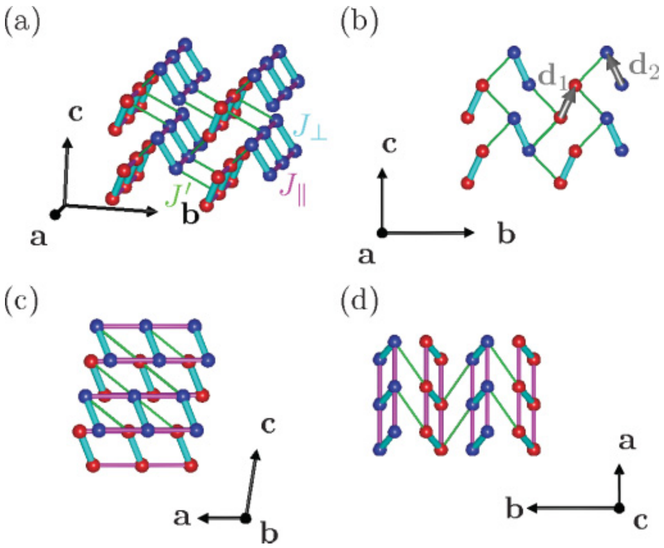

FIG. 18. (Color online) Coupling structure of BPCB where the unpaired electron spins of the Cu^{2+} atoms in the first (second) type of ladders are pictured by red (blue) spheres. The $J_\perp$, $J_\parallel$, and J' coupling paths are represented in turquoise, pink, and green, respectively. **a**, **b**, and **c** are the three unit-cell vectors of the structure. Gray arrows are the rung vectors of the two types of ladders $\mathbf{d}_{1,2}$. (a) 3D structure. (b) Projection of the 3D structure onto the **bc** plane. (c) Projection of the 3D structure onto the **ac** plane. (d) Projection of the 3D structure onto the **ab** plane.

$$h^z \rightarrow g\mu_B h^z \tag{40}$$

in Eq. (2), with μ_B being the Bohr magneton and g being the Landé factor of the unpaired copper electron spins. The latter depends on the orientation of the sample with respect to the magnetic field. For the orientation chosen in the NMR measurements,[30] it amounts to $g \approx 2.126$.[88] It can vary up to ~10% for other experimental setups.[28]

B. Thermodynamic measurements and low-energy properties

Many interesting thermodynamic measurements have been performed on BPCB. We select in the following some of these experiments and compare them to the theoretical predictions.

The longitudinal magnetization that can be measured very precisely by NMR (see Ref. 30) was shown to agree remarkably with the one computed using the weakly coupled ladder model (Fig. 3). Unfortunately, the magnetization is not very sensitive to the underlying model (see Sec. IV A). Thus it cannot be used to select between various models, but once the model is fixed, it can be used to fix precisely the parameters given the high accuracy of the experimental data. In particular, the position of the critical fields are very sensitive to the values of the intraladder couplings (Sec. IV A). The couplings determined by this method are $J_\perp \approx 12.6$ K and $J_\parallel \approx 3.55$ K.

A more selective test to distinguish between various models is provided by the specific heat. This is due to the fact that the specific heat contains information on high-energy excitations that are characteristic for the underlying model. As shown in Fig. 6, the experimental data are remarkably described, up to an accuracy of a few percent, by a simple Heisenberg ladder Hamiltonian with the parameters extracted from the magnetization. In particular, not only the low-temperature behavior is covered by the ladder description, but also the higher maxima. This indicates that the ladder Hamiltonian is an adequate description of the compound. The small discrepancies between the specific-heat data and the calculation, which is essentially exact, can have various sources. First, the substraction of the nonmagnetic term in the experimental data can account for some of the deviations. Furthermore, the interladder coupling can induce slight changes in the behavior of the specific heat. Finally, deviations from the simple ladder Hamiltonian can be present. Small anisotropy of the couplings can exist and indeed are necessary to interpret recent ESR experiments.[87] Other terms, such as longer-range exchanges or Dzyaloshinskii-Moryia (DM) terms, might occur along the legs even if the latter is forbidden by symmetry along the dominant rung coupling. Clearly all these deviations from the Heisenberg model cannot be larger than a few percent. They will not lead to any sizable deviation for the LL parameters (Fig. 23) in the 1D regime. Close to the critical points they can, however, play a more important role. It would thus be interesting in subsequent studies to refine the model to take such deviations into account.

After having fixed the model and the intraladder couplings up to a few percent, we use it to compute other experimentally accessible quantities such as the magnetostriction, thermal expansion, the NMR relaxation rate, the transition temperature to the ordered phase, and its order parameter. In Refs. 85 and 86 the magnetostriction and thermal expansion were compared to the theoretical results by using the described ladder model. A very good agreement was found in a broad range of temperatures (not shown here). Note that only a full ladder model allows a global quantitative description of the magnetostriction effect, which provides an additional confirmation of the applicability of the model. The quality of the determination of the model and its intraladder parameters becomes even more evident in the comparison of the NMR data for the relaxation rate T_1^{-1} with the theoretical results of the LL theory, as shown in Fig. 8. Only *one* adjustable parameter is left, namely, the hyperfine coupling constant (see Sec. IV C). This parameter allows for a global expansion of the theoretical curve, but not for a change of its shape. The agreement between the theory and the experimental data is very good over the whole range of the magnetic field and only small deviations can be seen. The compound BPCB thus allows to *quantitatively* test the LL universality class. Even though the LL description is restricted to low energies, in BPCB its range of validity is rather large. Indeed, at high energy, its breakdown is approximately signaled by the first peak of the specific heat[29] (see Sec. IV B 2). Here this has a maximum scale of $T \sim 1.5$ K at midpoint between h_{c1} and h_{c2} [see Fig. 5(c)]. Given the low ordering temperature, which has a maximum at approximately $T \sim 100$ mK, this leaves a rather large LL regime for this compound.

Taking now the coupling between ladders into account, one can induce a transition to a 3D-ordered phase. The transition temperature is shown in Fig. 9. Experimentally, it is determined by NMR[30] and ND measurements.[31] Theoretically the ladders are described by LL theory, and their interladder coupling is treated in a mean-field approximation (see Secs. III C and III D). As shown in Fig. 9, the LL theory provides a remarkable description of the transition to the transverse antiferromagnetic order at low temperatures. The shape of $T_c(h^z)$ is almost perfectly reproduced, in agreement with both the NMR[30] and the ND data.[31] The comparison with the experiments determines the interladder coupling J', the only adjustable parameter. The simple mean-field approximation would give a value of $J' \sim 20$ mK. As discussed in Sec. IV D 1, the mean field tends to underestimate the coupling, and it should be corrected by an essentially field-independent factor. Taking this into account, we obtain a coupling of the order of $J' = 27$ mK.

The order parameter in the antiferromagnetic phase can be observed also by experiments. It shows a very interesting shape. At a pure experimental level ND and NMR have some discrepancies, as shown in Fig. 10. These discrepancies can be attributed to the different temperatures at which the data has been taken, and a probable underestimate of the temperature in the ND experiments.[31] Indeed, the order parameter close to the critical magnetic field h_{c2} is very sensitive to temperature, because the transition temperature drops steeply in this regime. Note that, although the NMR allows clearly for a more precise measurement of the transverse staggered magnetization, it cannot give its absolute value. Thus the amplitude of the order parameter is fixed from the ND measurement. Even though a good agreement between the theoretical results and the experimental results is obtained, several questions concerning the deviations remain to be addressed.

First, the theoretical curve does not fully follow the shape of the experimental data. Particularly at high fields, the experimental data shows a stronger decrease. A simple explanation for this effect most likely comes from the fact that the calculation is performed at zero temperature, while the measurement is done at 40 mK. This is not a negligible temperature with respect to T_c, in particular, at magnetic fields close to h_{c2}. Extrapolation of the experimental data to zero temperature[30] improves the agreement. However, for a detailed comparison, either lower-temperature measurements or a calculation of the transverse staggered magnetization at finite temperature would be required. Both are quite difficult to perform and will clearly require further studies.

The second question comes from the amplitude of the staggered magnetization. Indeed, the experimental data seem to be slightly above the theoretical curve, even if one uses the value $J' = 27$ mK for the interladder coupling. This is surprising because one would expect that going beyond the mean-field approximation could only reduce the order parameter. Naively, one would thus need a larger coupling, perhaps of the order of $J' \sim 60$–80 mK, to explain the amplitude of the order parameter. This is a much larger value than the one extracted from the comparison of T_c. How to reconcile these two values remains open. The various anisotropies and additional small perturbations in the ladder Hamiltonian could resolve part of this discrepancy. However, it seems unlikely that they result in a correction of J' by a factor of ~2–3. Another origin might be the presence of some level of frustration present in the interladder coupling. Clearly more experimental and theoretical studies are needed on that point.

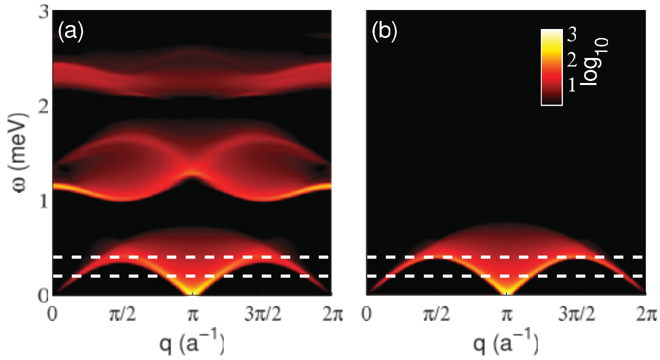

FIG. 19. (Color online) Theoretical momentum-energy-dependent INS cross section for BPCB with $\mathbf{Q}\cdot\mathbf{d}_i=\pi$ $(i=1,2)$ and $q=\mathbf{Q}\cdot\mathbf{a}$ at $m^z=0.5$ in (a) a ladder system and (b) the spin chain mapping. The horizontal dashed lines correspond to the constant energy scans at $\omega=0.2$ and 0.4 meV shown in Fig. 21.

C. Inelastic neutron scattering (INS)

The INS technique is a direct probe for dynamical spin-spin correlation functions. Measurements have been performed on the compound BPCB in the spin liquid phase[32,33] (low magnetic field) and in the gapless regime.[32] By modeling the compound BPCB with two inequivalent uncoupled ladders oriented along the two rung vectors $\mathbf{d}_{1,2}$ (see Fig. 18), the magnetic INS cross section[89] is given by the formula

$$\frac{d^2\sigma}{d\Omega\, dE'} \propto \frac{q'}{q}|F(\mathbf{Q})|^2 \sum_{i=1,2}\left\{\frac{1}{2}\left(1+\frac{Q^{z2}}{\mathbf{Q}^2}\right)\right. \times [\cos(\mathbf{Q}\cdot\mathbf{d}_i)\,(S_{21}^{+-}+S_{21}^{-+})+S_{11}^{+-}+S_{11}^{-+}] \left. +2\left(1-\frac{Q^{z2}}{\mathbf{Q}^2}\right)\left[\cos(\mathbf{Q}\cdot\mathbf{d}_i)S_{21}^{zz}+S_{11}^{zz}\right]\right\}. \quad (41)$$

Here $\mathbf{Q}=(Q^x,Q^y,Q^z)=\mathbf{q}-\mathbf{q}'$ is the momentum transferred to the sample ($\mathbf{q}$ and $\mathbf{q}'$ are the incident and scattered neutron momenta, respectively) and $\omega=E-E'$ is the transferred energy (E and E' are the incident and scattered neutron energies, respectively). The correlations $S_{ij}^{\alpha\beta}$ are understood to be evaluated at the momentum $\mathbf{Q}\cdot\mathbf{a}$ and frequency ω, and are defined by

$$S_{ij}^{\alpha\beta}(\mathbf{Q}\cdot\mathbf{a},\omega)=\frac{S_0^{\alpha\beta}(\mathbf{Q}\cdot\mathbf{a},\omega)\pm S_\pi^{\alpha\beta}(\mathbf{Q}\cdot\mathbf{a},\omega)}{2} \qquad (42)$$

(the + sign if $i=j$ and the − sign if $i\neq j$), with $S_{q_y}^{\alpha\beta}$ defined at zero temperature in Eq. (31) and evaluated for a momentum $q=\mathbf{Q}\cdot\mathbf{a}$ along the **a** unit-cell vector (momentum along the ladder direction). The magnetic form factor $F(\mathbf{Q})$ of the Cu^{2+} and the ratio q'/q are corrected in the experimental data.

The INS cross section (41) is directly related to a combination of different correlation functions $S_{q_y}^{\alpha\beta}$ with weights depending on the transferred momentum **Q** and the magnetic-field orientation. In the model definition (see Sec. II A), the magnetic field **h** is pointing along the z direction. Aligning it to the **b** unit-cell vector and tuning **Q** in the $\mathbf{a}^\star\mathbf{c}^\star$ plane ($\mathbf{a}^\star$, $\mathbf{b}^\star$, and $\mathbf{c}^\star$ are the reciprocal vectors of **a**, **b**, and **c**) allows one to keep constant the prefactors in Eq. (41) scanning the $\mathbf{a}^\star$ momenta with the condition $\mathbf{Q}\cdot\mathbf{d_i}=0$ or π to target the symmetric or antisymmetric part, respectively.

We focus here on the antisymmetric part for which the low-energy spectra already have been studied experimentally and theoretically.[32] Theoretically, the focus so far lay on the description by the spin chain mapping. We compute here the INS cross section (41) for the full ladder at $m^z=0.25$, 0.5, and 0.75 by using the correlations presented in Sec. V. The results are shown in Figs. 19 and 20 and are compared to the results from the spin chain mapping.

As expected from expression (41), it contains the different excitations present in the spectra of S_π^{zz} and $S_\pi^{\pm\mp}$ [cf. Figs. 12(b), 13(b), and 14(b)]:

(a) The low-energy continuum originates from the transversal correlations $S_\pi^{\pm\mp}$. It is qualitatively well described by the spin chain mapping that presents a symmetry with respect to half magnetization.

(b) The continuum of excitations at energy[83] $\sim J_\perp$ comes from the longitudinal correlation S_π^{zz} and is not present in the spin chain mapping.

(c) The continuum of excitations at energy[83] $\sim 2J_\perp$ comes from the transversal correlation S_π^{+-} and is not present in the spin chain mapping.

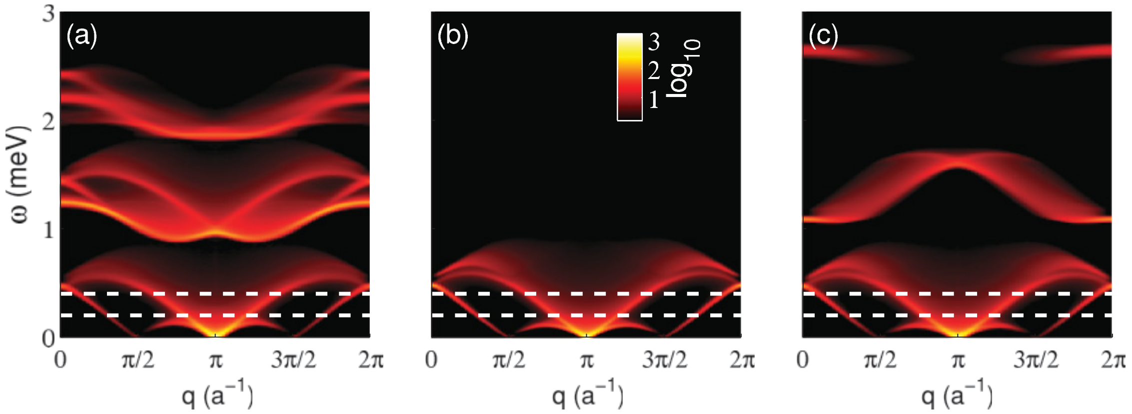

FIG. 20. (Color online) Theoretical momentum-energy-dependent INS cross section for BPCB with $\mathbf{Q}\cdot\mathbf{d}_i=\pi$ $(i=1,2)$ and $q=\mathbf{Q}\cdot\mathbf{a}$ at (a) $m^z=0.25$, (b) $m^z=0.25,0.75$ in the spin chain mapping, and (c) $m^z=0.75$. The horizontal dashed lines correspond to the constant energy scans at $\omega=0.2$ and 0.4 meV plotted in Fig. 22.

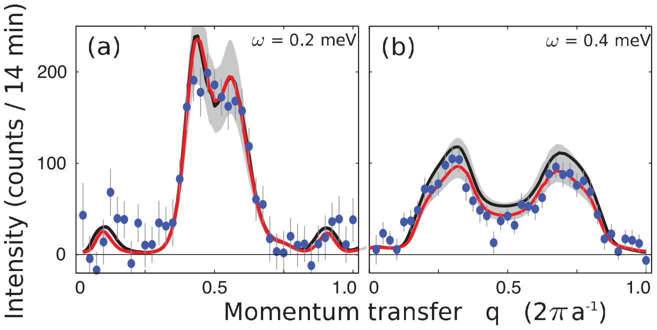

FIG. 21. (Color online) INS intensity measured along $\mathbf{a}^{\star}$ of BPCB (Ref. 32) with the momentum π in the rung direction ($\mathbf{Q} \cdot \mathbf{d_i} = \pi$) at $h^z = 10.1$ T ($m^z \approx 0.5$) and $T = 250$ mK after substraction of the zero-field background. In each panel, fixed energy scans (shown by white dashed lines in Fig. 19) are plotted: (a) $\omega = 0.2$ meV, (b) $\omega = 0.4$ meV. The circles correspond to the experimental data. The red (black) solid lines are the $m^z = 0.5$ theoretical data for the ladder (the spin chain mapping) convolved with the instrumental resolution. The shaded bands indicate the error bar in the experimental determination of a single proportionality constant valid for all fields, energies, and wave vectors. The width of these areas combines the statistics of all our scans with uncertainties in the exact magnetization values at the chosen fields and in the convolution procedure.

The main features of the low-energy continuum (a) are well covered by the spin chain mapping.[32] However, slight differences between the low-energy excitations in the spin ladder and the spin chain are still visible (cf. also Sec. V C 2). They can even be distinguished in the experimental data as shown in Figs. 21 and 22, where some cuts at fixed energy $\omega = 0.2$ and 0.4 meV are plotted. The INS measured intensity is directly compared to the theoretical cross section (41) computed for the ladder and the spin chain mapping at $m^z = 0.24$, 0.5, and 0.72 convolved with the instrumental resolution. The amplitude is fixed by fitting one proportionality constant for all fields, energies, and wave vectors.

These scans at fixed energy present peaks when the lower edge of the continua (related to the correlations $S_\pi^{\pm\mp}$) is crossed (see the dashed white lines in Figs. 19 and 20). As one can see, the theoretical curves for the ladder and the spin chain both reproduce well the main features in the experimental data and only small differences are present:

(i) The spectral weight intensity at $m^z = 0.5$ and $\omega = 0.4$ meV [in Fig. 21(b)] is slightly overestimated by the spin chain mapping.

(ii) The height of the two central peaks at $m^z = 0.24$ and $\omega = 0.2$ meV [in Fig. 22(c)] is underestimated by the spin chain mapping.

Whereas the low-energy excitations (a) only showed a slight asymmetry with respect to the magnetization, a very different behavior can be seen in the high-energy part (b) and (c). Indeed, the high-energy part of the INS cross section (Fig. 20) is very asymmetric with respect to half magnetization. As we discussed in Sec. V, these excitations are due to the high-energy triplets that can be excited in S_π^{zz} and S_π^{+-} [see Figs. 12(b) and 13(b)] and are totally neglected in the spin chain mapping. Their corresponding spectral weight is of the same order than the low-energy spectra, and thus should be accessible experimentally. It would be very interesting to have an experimental determination of this part of the spectrum, because as we have seen it contains characteristic information on the system itself and is related to itinerant systems via the various mappings.

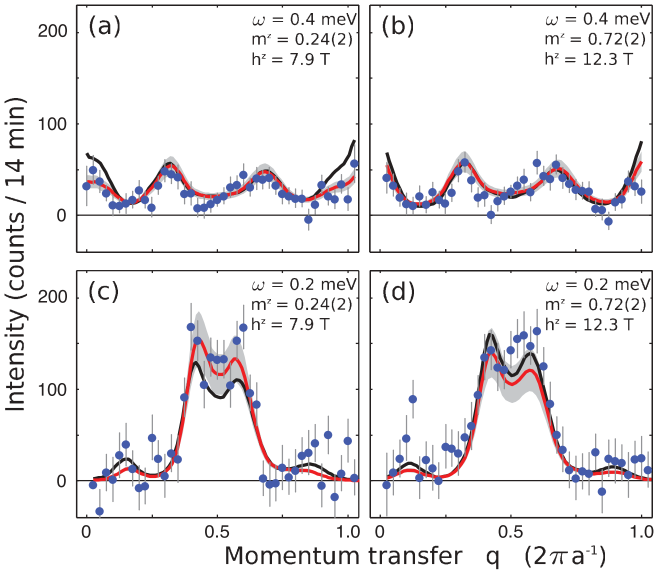

FIG. 22. (Color online) INS intensity measured along $\mathbf{a}^{\star}$ of BPCB (Ref. 32) with a π momentum in the rungs ($\mathbf{Q} \cdot \mathbf{d_i} = \pi$) at $T = 250$ mK after substraction of the zero-field background. In each panel, cuts at fixed energy (shown by white dashed lines in Fig. 20) are plotted: (a) $\omega = 0.4$ meV and $m^z = 0.24$, (b) $\omega = 0.4$ meV and $m^z = 0.72$, (c) $\omega = 0.2$ meV and $m^z = 0.24$, and (d) $\omega = 0.2$ meV and $m^z = 0.72$. The circles correspond to the experimental data. The solid red (black) curves are the theoretical data for the ladder (the spin chain mapping) convolved with the instrumental resolution. The shaded bands indicate the error bar in the experimental determination of a single proportionality constant valid for all fields, energies, and wave vectors. The width of these areas combines the statistics of all our scans with uncertainties in the exact magnetization values at the chosen fields and in the convolution procedure.

VII. CONCLUSIONS

In this paper we have looked at the thermodynamic and dynamical properties of weakly coupled spin ladders under a magnetic field. This was done by a combination of analytical techniques, such as BA, bosonization, and LL theory, and numerical techniques such as DMRG and QMC. Using this combination of techniques we were able to explore the physical properties in the three main regions of the phase diagram of such spin ladders under a magnetic field, namely, (a) a gapped spin liquid at low fields, (b) a massless phase at intermediate fields $h_{c1} < h^z < h_{c2}$, and (c) a saturated phase at larger fields. In addition to the theoretical analysis, we compared our findings to the experimental results on the compound BPCB $[(C_5H_{12}N)_2CuBr_4]$, which is an excellent realization of such ladder systems.

For thermodynamics we computed the magnetization and specific heat of the system as a function of temperature and magnetic field. The extension of the DMRG technique to finite temperature allows us to compute these quantities with excellent accuracy. In the gapless phase the low-energy part of the specific heat agrees well with the prediction of the LL theory, which is the low-energy theory describing most of the massless 1D systems. At higher temperatures, the numerical solution is needed to capture the precise structure of the peaks in the specific heat that reflect the presence of the excited states in the ladder. Comparison of the theoretical calculations with the measured magnetization and specific heat proves to be remarkable. This good agreement confirms that the ladder model is indeed a faithful description of the compound BPCB. It also gives direct access, via the maxima in magnetization and peaks in the specific heat, to the approximate region of applicability of the LL description. For the low-energy dynamics we used a combination of the numerical techniques to determine the LL parameters and then the analytical description based on LL to compute the dynamical spin-spin correlation functions. This allowed to extract the NMR relaxation rate and the 1D antiferromagnetic transverse susceptibility. If the ladders are very weakly coupled, which is the case in the considered material, the divergence of the susceptibility leads to a 3D antiferromagnetic order at low temperatures in the direction transverse to the applied magnetic field. We computed this transition temperature and the order parameter at zero temperature. Comparison with the measured experimental quantities both by NMR and ND proved again to be remarkable. This excellent agreement between theory and experiment for these quantities as a function of the magnetic field allows to *quantitatively* test the LL theory. Indeed, it shows that several different correlations are described totally by the knowledge of the two LL parameters (and the amplitudes relating the microscopic operators to the field theory one). This is something that could not be really tested previously because either the microscopic interactions were not known in detail, leaving the LL parameters as adjustable parameters, or only one correlation function could be measured in a given experiment, not allowing to test for universality of the description.

We also gave a detailed description of the dynamical spin-spin correlations, for $T = 0$ using the t-DMRG method, for a wide range of energies and all momenta. The excitations reveal much important information on the system and are well suited to characterize it. In particular, we show the interesting evolution of the excitations in the system with the magnetic field and with different coupling strengths. Quite interestingly, the intermediate energy part can be related to the excitations of a t-J model and thereby shows features of itinerant systems. We also showed that the dynamical correlations of the ladder posses characteristic high-energy features that are clearly distinct from the corresponding spectrum for spin chains.

The numerical calculation is efficient for the high- and intermediate-energy part of the spectrum for which the LL description cannot be applied. We showed that the two methods, numerics and LL, have enough overlap, given the accuracy of our calculation, so that we can have a full description of the dynamical properties at all energies. This allowed us to use each of the methods in the regime where it is efficient. In particular, in the present study we did not push the numerical calculations to try to obtain the exact behavior at low energies, but focused on the high- and intermediate-energy regime. We used the analytical description coupled to the numerical determination of the LL parameters to obtain a very accurate low-energy description. We made the connection between our results and several analytical predictions. In particular, at intermediate or low energy our calculation agrees with the LL prediction of incommensurate points and behavior (divergence and convergence) of the correlations.

We compared our numerical results with existing INS data on the compound BPCB and found excellent agreement. It is rewarding to note that the resolution of our dynamical calculation is, in energy and momentum, at the moment better than the one of the experiment. The comparison between theory and experiment is thus essentially free of numerical error bars. Given the current resolution of the INS experiment, it is difficult to distinguish in the low-energy part of the spectrum the difference between the dynamical correlation of the true ladder and the one of an anisotropic spin-$1/2$ system, which corresponds to the strong rung exchange limit. More accurate experiments would be desirable in this respect. An alternative route is to probe experimentally the high-energy part of the spectrum, because these high-energy excitations contain many characteristic features of the underlying model.

On the conceptual side and also in connection with the compound BPCB, several points remain to be investigated. An extension of the dynamical results to finite temperature would be desirable. This could be used to study different effects such as the interesting shifts and damping of the triplet modes with temperature that have been observed in 3D gapped systems.[90] A second important step would be to improve the description of the quasi-1D systems, by including in a mean-field way the effect of the other ladders in the numerical study. This is something we already partly performed, but the extension to the dynamical quantities remains to be done. This is specially important close to the quantum critical points h_{c1} and h_{c2}, where the interladder coupling becomes crucial and the system undergoes a dimensional crossover between a 1D and a higher-dimensional (3D typically) behavior. Understanding such a crossover is a particularly challenging question because the system goes from a description for which an image of essentially free fermions applies (in the 1D regime) to one for which a description in terms of essentially free bosons (the 3D regime) applies.

One step further would be the extension of the investigation of the combined numerical–analytical methods we used here to other systems, including ladder systems with certain asymmetries or in the presence of disorder.

ACKNOWLEDGMENTS

We thank T. Barthel, C. Berthod, J.-S. Caux, V. V. Cheianov, A. Furusaki, U. Schollwöck, S. Trebst, and S. White for useful discussions, and especially J.-S. Caux for the data exchange. We acknowledge support of the “Triangle de la Physique,” the ANR “FAMOUS,” and of the Swiss NSF, under MaNEP and Division II. T.G. would like to thank the Aspen Center for Physics, where part of this work was completed. M.K. acknowledges support from the Centre of Excellence EN → FIST, Dunajska 156, SI-1000 Ljubljana, Slovenia.

APPENDIX A: STRONG COUPLING EXPANSION OF A SINGLE SPIN LADDER

In this Appendix we show how the spin ladder Hamiltonian (2) at strong coupling ($\gamma \ll 1$) can be expressed in bosonic operators acting on single bonds introduced in Ref. 91. This representation allows a classification of the excitations due to their position in energy. We first derive perturbatively an effective system based on this Hilbert space organization by energy sectors. We introduce the Schrieffer-Wolff transformation that maps the physical system to the effective system, and approximate it by using a strong coupling expansion. Thus, we evaluate the rung densities of the ground state in the spin liquid, and derive an effective theory for the gapless regime. Furthermore, we evaluate the deviation of the LL parameters from the spin chain mapping.

1. Strong coupling expansion

The four-dimensional Hilbert space on each rung l is spanned by the states $|s\rangle$, $|t^+\rangle$, $|t^0\rangle$, and $|t^-\rangle$ [cf. Eqs. (9) and (10)], obtained by applying the boson creation operators $s_l^\dagger$, $t_{l,+}^\dagger$, $t_{l,0}^\dagger$, and $t_{l,-}^\dagger$ to a vacuum state. A hardcore boson constraint applies on each rung l, i.e.,

$$\varrho_{l,s} + \varrho_{l,+} + \varrho_{l,0} + \varrho_{l,-} = 1, \tag{A1}$$

where $\varrho_{l,s} = s_l^\dagger s_l$ and $\varrho_{l,k} = t_{l,k}^\dagger t_{l,k}$, $k = \pm, 0$.

While the Hamiltonian on the rung $H_\perp$ (3) is quadratic in the boson operators,

$$H_\perp = \sum_{l=1}^{L} [(1 - h^z/J_\perp)\varrho_{l,+} + \varrho_{l,0} + (1 + h^z/J_\perp)\varrho_{l,-}] - \frac{3}{4}L, \tag{A2}$$

the chain Hamiltonian $H_\parallel$ (4) is quartic, and its structure is quite complex. The advantage of the boson representation is revealed when considering the case of small γ. In that case we perform a Schrieffer-Wolff transformation of the spin ladder Hamiltonian (2),

$$H_{\text{eff}} = e^{i\gamma A} H e^{-i\gamma A}. \tag{A3}$$

The Hermitian operator A can be expanded in powers of γ,

$$A = A_1 + \gamma A_2 + \cdots. \tag{A4}$$

Thus H_{eff} can be written in orders of γ as

$$J_\perp^{-1} H_{\text{eff}} = H_\perp + \gamma H^{(1)} + \gamma^2 H^{(2)} + \cdots, \tag{A5}$$

where

$$H^{(1)} = H_\parallel + i[A_1, H_\perp], \tag{A6}$$

$$H^{(2)} = i[A_2, H_\perp] - \tfrac{1}{2}[A_1, [A_1, H_\perp]] + i[A_1, H_\parallel], \tag{A7}$$

etc. Through this expansion, the unitary transform $e^{i\gamma A}$ can be perturbatively determined by computing the A_k recursively in order to eliminate the transitions between the energy sectors of excitations in H_{eff}. Since the first term $J_\perp H_\perp$ in Eq. (A5) leads to a separation of excitations on the order of the energy scale $J_\perp$ [cf. Fig. 2(a)], the decoupled bond limit provides the effective Hilbert space that contributes to each energy sector. The second term $J_\parallel H^{(1)}$ causes broadening of these bands on the order of $J_\parallel$ and can induce a complex structure within the energy bands. To obtain the desired expansion up to the first order in γ, we choose

$$A_1 = \frac{i}{4} \sum_l s_l^\dagger s_{l+1}^\dagger (t_{l,0} t_{l+1,0} - t_{l,+} t_{l+1,-} - t_{l,-} t_{l+1,+}) + \text{H.c.}, \tag{A8}$$

where H.c. stands for the Hermitian conjugation.

2. Rung state density in the spin liquid

In the spin liquid phase, the decoupled bond limit provides the effective ground state $|0_{\text{eff}}\rangle = |s \cdots s\rangle$, which is related to the physical ground state by

$$|0\rangle = e^{-i\gamma A} |0_{\text{eff}}\rangle. \tag{A9}$$

So the triplet density of the ground state $\langle \rho_k \rangle$ (with $k = \pm, 0$) is given by

$$\langle \rho_k \rangle = \langle \varrho_{l,k} \rangle = \langle s \cdots s | e^{i\gamma A} \varrho_{l,k} e^{-i\gamma A} | s \cdots s \rangle. \tag{A10}$$

Using Eq. (A8), and keeping only the nonvanishing corresponding terms in (A10) up to second order, we get

$$\langle \rho_k \rangle \cong \gamma^2 \langle s \cdots s | A_1 \varrho_{l,k} A_1 | s \cdots s \rangle = \frac{\gamma^2}{8}. \tag{A11}$$

In the case of the compound BPCB (see Sec. VI A) this expansion gives $\langle \rho_k \rangle \cong 0.01$, and due to the hardcore boson constraint [Eq. (A1)] $\langle \rho_s \rangle = \langle \varrho_{l,s} \rangle \cong 0.97$. Even though we took into account only the first-order term for A in Eq. (A4), this approximation of the triplet density differs from the direct numerical computations (in Fig. 4) of only ~20%.

3. Effective Hamiltonian in the gapless regime

The first-order term $H^{(1)}$ of the effective Hamiltonian (A5) is computed by substituting (A8) into (A6). This leads to $H^{(1)}$ in the form

$$H^{(1)} = \sum_{k=0}^{4} \underbrace{\frac{1}{2} \sum_l \mathcal{H}_{k,l}^{(1)}}_{=H_k^{(1)}}, \tag{A12}$$

where

$$\mathcal{H}_{0,l}^{(1)} = s_{l+1}^\dagger t_{l,+}^\dagger t_{l+1,+} s_l + \tfrac{1}{2} \varrho_{l+1,+} \varrho_{l,+} + \text{H.c.}, \tag{A13}$$

$$\mathcal{H}_{1,l}^{(1)} = s_{l+1}^\dagger t_{l,0}^\dagger t_{l+1,0} s_l + t_{l+1,+}^\dagger t_{l,0}^\dagger t_{l+1,0} t_{l,+} + \text{H.c.}, \tag{A14}$$

$$\begin{aligned} \mathcal{H}_{2,l}^{(1)} = {} & s_{l+1}^\dagger t_{l,-}^\dagger t_{l+1,-} s_l - \tfrac{1}{2}(\varrho_{l+1,+} \varrho_{l,-} + \varrho_{l+1,-} \varrho_{l,+}) \\ & + t_{l+1,0}^\dagger t_{l,0}^\dagger t_{l+1,-} t_{l,+} + t_{l+1,0}^\dagger t_{l,0}^\dagger t_{l+1,+} t_{l,-} + \text{H.c.}, \end{aligned} \tag{A15}$$

$$\mathcal{H}_{3,l}^{(1)} = t_{l+1,0}^\dagger t_{l,-}^\dagger t_{l+1,-} t_{l,0} + \text{H.c.}, \tag{A16}$$

and

$$\mathcal{H}_{4,l}^{(1)} = \varrho_{l+1,-} \varrho_{l,-}. \tag{A17}$$

Here we regrouped the terms such that each $J_\perp H_k^{(1)}$ acts on the corresponding energy sector $kJ_\perp$, $k = 0, 1, \ldots, 4$ in the gapless regime. Note that in each sector $A_1 = 0$ such that to the considered order in γ the Hamiltonian (2) corresponds to the effective Hamiltonian.

a. Low-energy sector

When focusing on the low-energy sector, the $|s\rangle$ and the $|t_+\rangle$ modes dominate the behavior and we can assume a vanishing density of $|t_0\rangle$ and $|t_-\rangle$ triplets. Thus the hardcore boson constraint (A1) simplifies to

$$\varrho_{l,s} + \varrho_{l,+} = 1 \tag{A18}$$

and the rung Hamiltonian (A2) simplifies to

$$H_\perp = (1 - h^z/J_\perp)\sum_l \varrho_{l,+} - \frac{3}{4}L. \tag{A19}$$

Further, the only contribution to the first-order term in γ comes from $H_0^{(1)}$. Taking this into account, we obtain from Eq. (A5) for the Hamiltonian (2) in the lowest energy sector

$$H = J_\perp H_\perp + J_\parallel H_0^{(1)}, \tag{A20}$$

where $H_\perp$ is given by Eq. (A19) and $H_0^{(1)}$ by Eq. (A13). Following Ref. 17, we map the two low-energy modes on the two states of a pseudospin [Eq. (11)], and replace the boson operators $s^\dagger$ and $t_+^\dagger$ with the spin-1/2 operators,

$$\tilde{S}_l^+ = t_{l,+}^\dagger s_l, \quad \tilde{S}_l^- = s_l^\dagger t_{l,+}, \quad \tilde{S}_l^z = \varrho_{l,+} - \tfrac{1}{2}. \tag{A21}$$

The effective Hamiltonian is the spin-1/2 *XXZ* Heisenberg Hamiltonian, Eq. (13).

b. Sector of energy $J_\perp$

The effective Hilbert space of the $J_\perp$ energy sector corresponds to a single $|t^0\rangle$ triplet excitation lying in a sea of singlets $|s\rangle$ and triplets $|t^+\rangle$. The effective Hamiltonian up to first order in γ is given by

$$H = J_\perp H_\perp + J_\parallel\big[H_0^{(1)} + H_1^{(1)}\big]. \tag{A22}$$

The excitation $|t^0\rangle$ can be interpreted as a single hole excitation in a spin chain formed by $|s\rangle$ and $|t^+\rangle$. Each rung state of this sector is identified with

$$|\tilde{\downarrow}\rangle = |s\rangle, \quad |\tilde{\uparrow}\rangle = |t^+\rangle, \quad |0\rangle = |t^0\rangle. \tag{A23}$$

In this picture the Hamiltonian (A22) can be mapped onto the anisotropic *t-J* model,

$$H_{t-J} = H_{XXZ} + H_t + H_{\text{s-h}} + \epsilon, \tag{A24}$$

where $\epsilon = (J_\perp + h^z)/2$ is an energy shift.

The hopping term

$$H_t = \frac{J_\parallel}{2}\sum_{l,\sigma}(c_{l,\sigma}^\dagger c_{l+1,\sigma} + c_{l+1,\sigma}^\dagger c_{l,\sigma}) \tag{A25}$$

stems from the term $J_\parallel H_1^{(1)}$ in Eq. (A22). Here $c_{l,\sigma}^\dagger$ ($c_{l,\sigma}$) is the creation (annihilation) operator of a fermion with pseudospin $\sigma = \tilde{\uparrow},\tilde{\downarrow}$ at the site l. Note that, although here we are dealing with spin states, it is possible to represent faithfully the three states of each site's Hilbert space ($|s\rangle$, $|t^+\rangle$, $|t^0\rangle$) using a fermion representation.

Additionally, a nearest-neighbor density-density term between the up spin and the hole arises:

$$H_{\text{s-h}} = -\frac{J_\parallel}{4}\sum_l (n_{l,\text{h}} n_{l+1,\tilde{\uparrow}} + n_{l,\tilde{\uparrow}} n_{l+1,\text{h}}). \tag{A26}$$

Here $n_{l,\text{h}}$ is the density operator of the hole at site l. This term stems from the nearest-neighbor interaction between the $|t_+\rangle$ triplets, i.e., the second term in Eq. (A13). Mapping this term onto a spin chain in the presence of a hole leads to an interaction term between the hole and the spin-up state. Note that this is in contrast to the usual mapping on a spin chain without a hole, in which case it would only cause a shift in energy.

4. Second-order perturbation and LL parameters

The second-order term $H^{(2)}$ (A7) of the expansion (A5) contains a huge amount of terms. Nevertheless, considering the low-energy sector, only the following terms,

$$\begin{aligned} H_0^{(2)} = &-\frac{3}{8}\sum_l \varrho_{l,s}\varrho_{l+1,s} \\ &-\frac{1}{8}\sum_l (t_{l-1,+}s_{l-1}^\dagger \varrho_{l,s} t_{l+1,+}^\dagger s_{l+1} + \text{H.c.}), \end{aligned} \tag{A27}$$

are important. The first term in Eq. (A27) is a singlet density-density interaction that can be absorbed into the coupling of the *XXZ* chain, and the second term is a conditionnal hopping.[92] In order to study the effects of $H_0^{(2)}$ on the LL parameters u and K (see Fig. 23), we first replace the boson operators with the spin-1/2 operators [Eq. (A21)]. So the Hamiltonian (2) in the low-energy sector becomes

$$H = H_{XXZ} - \frac{1}{8}\sum_l\left[\tilde{S}_{l-1}^-\left(\frac{1}{2} - \tilde{S}_l^z\right)\tilde{S}_{l+1}^+ + \text{H.c.}\right] + \text{const}, \tag{A28}$$

where H_{XXZ} is the *XXZ* Heisenberg chain Hamiltonian [Eq. (13)] with the corrected parameters

$$\Delta^{(2)} = \tfrac{1}{2} - \tfrac{3}{8}\gamma, \quad \tilde{h^z}^{(2)} = \tilde{h}^z - \tfrac{3}{8}J_\perp\gamma^2, \tag{A29}$$

up to the second order in γ. For the BPCB parameters [Eq. (15)] $\Delta^{(2)} \cong 0.4$ instead of $\Delta = 0.5$ for the spin chain mapping (first-order approximation). The LL parameters u, K, and A_x of H_{XXZ} with the anisotropy $\Delta^{(2)}$ are computed, and we treat the three-terms interaction (conditional hopping) by approximating $1/2 - \tilde{S}_l^z \cong 1/2 - \tilde{m}^z$ (mean-field approximation). The remaining term is then bosonized using the expression (17) for $\tilde{S}^\pm(x = l)$. It leads to the corrected LL parameter $\tilde{u}$ and $\tilde{K}$ of the Hamiltonian (A28) through the relations

$$\tilde{u}\tilde{K} = uK + 2\pi\gamma^2 J_\perp A_x(1/2 - \tilde{m}^z), \quad \tilde{u}/\tilde{K} = u/K. \tag{A30}$$

The corrected $\tilde{u}$ and $\tilde{K}$ are plotted in Fig. 23 and clearly show the asymmetric signature of the full ladder parameters induced by the conditional hopping term in (A28). Note that the lack of convergence $K \to 1$ when $m^z = \tilde{m}^z + 1/2 \to 0$ is obviously an artefact of the mean-field approximation $1/2 - \tilde{S}_l^z \cong 1/2 - \tilde{m}^z$ and the large sensitivity in the K determination with the ratio of Eq. (A30).

APPENDIX B: LUTTINGER LIQUID

In the following, we present several properties of the LL, providing a quantitative description of the low-energy physics

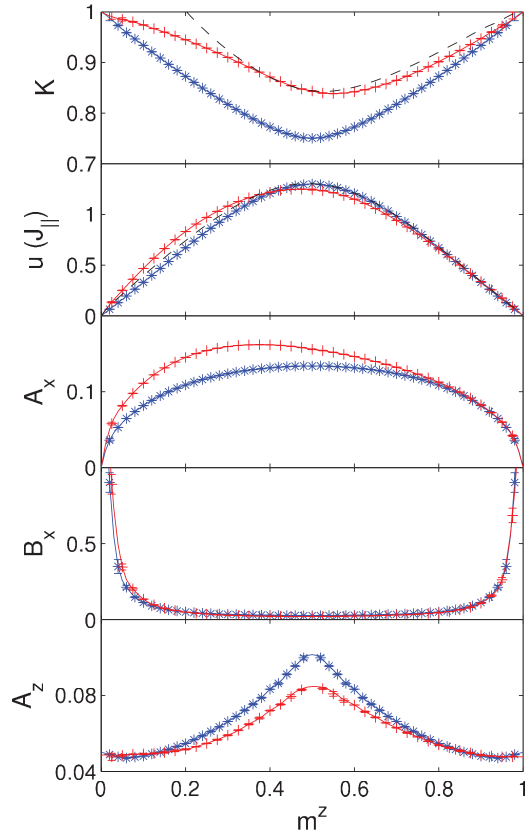

FIG. 23. (Color online) LL parameters u, K, and the prefactors of the spin operators A_x, B_x, and A_z vs the magnetization per rung m^z computed for a spin ladder with the BPCB couplings (39) (red crosses) and for the spin chain mapping (blue stars). The strong coupling expansion of u and K up to the second order in γ (discussed in Appendix A 4) is plotted as black dashed lines.

of the gapless regime in the spin ladder model (2) and the spin chain mapping (13). We start with the determination of the parameters that characterize totally the LL description. Then we summarize the spin-spin correlation functions deduced from the LL theory at zero and finite temperature.

1. LL parameter determination

In this section we detail the determination of the LL parameters u and K, and the prefactors A_x, B_x, and A_z [see Eqs. (16), (17), and (18), respectively]. The parameters K, A_x, B_x, and A_z and their dependence on the magnetic field have been determined previously in Refs. 25, 26, and 93 for different values of the couplings than considered here. We obtain these parameters in two steps:[30,94]

(i) We determine the ratio u/K from its relation to the static susceptibility [Eq. (B1)], which is a quantity numerically easily accessible with DMRG or BA (for the spin chain only).

(ii) The parameters K and the prefactors A_x, B_x, and A_z are extracted by fitting numerical results for the static correlation functions obtained by DMRG with their analytical LL expression. For the spin chain, it is also possible to deduce the product uK from the magnetic stiffness computed by BA.[6,95]

We give the relations used for the spin chains only, because from these the relations for the spin ladders can be inferred easily by using the following relations:

$$m^z \to \tilde{m}^z + \frac{1}{2}, \quad \frac{\partial m^z}{\partial h^z} \to \frac{\partial \tilde{m}^z}{\partial \tilde{h}^z},$$

$$\langle S^x_{l,\pi} S^x_{l',\pi}\rangle \to 2\langle \tilde{S}^x_l \tilde{S}^x_{l'}\rangle, \quad \langle S^z_{l,0}\rangle \to \langle \tilde{S}^z_l\rangle + \frac{1}{2},$$

$$\langle S^z_{l,0} S^z_{l,0'}\rangle \to \langle \tilde{S}^z_l \tilde{S}^z_{l'}\rangle + \frac{1}{2}\left(\langle \tilde{S}^z_l\rangle + \langle \tilde{S}^z_{l'}\rangle\right) + \frac{1}{4}.$$

a. Susceptibility and u/K

The LL theory predicts that the static susceptibility $\frac{\partial \tilde{m}^z}{\partial \tilde{h}^z}$ is related to the ratio u/K through the relation[6,95]

$$\frac{u}{K} = \frac{1}{\pi \frac{\partial \tilde{m}^z}{\partial \tilde{h}^z}}. \tag{B1}$$

We numerically compute the static susceptibility by using DMRG or BA (for the spin chain only) and infer the ratio u/K with a negligible error.

b. Static correlation functions

For the extraction of the parameters K, A_x, B_x, and A_z, we fit numerical DMRG results for the correlation functions $\langle \tilde{S}^x_l \tilde{S}^x_{l'}\rangle$, $\langle \tilde{S}^z_l \tilde{S}^z_{l'}\rangle$, and the local magnetization $\langle \tilde{S}^z_l\rangle$ with their analytical expression for finite system size, Eqs. (11), (12), and (13) in Ref. 26, respectively. In the limit of infinite system size and far from the boundaries, these LL correlations simplify to the well-known power-law decay

$$\langle \tilde{S}^x_l \tilde{S}^x_{l'}\rangle = A_x \frac{(-1)^{l-l'}}{|l-l'|^{\frac{1}{2K}}} - B_x (-1)^{l-l'} \frac{\cos[q(l-l')]}{|l-l'|^{2K+\frac{1}{2K}}}, \tag{B2}$$

$$\langle \tilde{S}^z_l \tilde{S}^z_{l'}\rangle = \tilde{m}^{z\,2} + A_z (-1)^{l-l'} \frac{\cos[q(l-l')]}{|l-l'|^{2K}} - \frac{K}{2\pi^2 |l-l'|^2}, \tag{B3}$$

and the local magnetization becomes constant, $\langle \tilde{S}^z_l\rangle = \tilde{m}^z$.

We first fit the transverse correlation (xx-correlation $\langle \tilde{S}^x_l \tilde{S}^x_{l'}\rangle$) to extract the parameters K, A_x, and B_x. Then we use the previously extracted value for K to fit the longitudinal correlation (zz-correlation $\langle \tilde{S}^z_l \tilde{S}^z_{l'}\rangle$) and the magnetization, $\langle \tilde{S}^z_l\rangle$, which allow us to determine A_z. The values determined by both fits are very close, and in Fig. 23 the average value of both is shown.

All the results presented in Fig. 23 were done for $L = 200$ and several hundred DMRG states after an average on the four sets of used data points in the fit $10 < l,l' < 170$, $30 < l,l' < 170$, $10 < l,l' < 190$, and $30 < l,l' < 190$. The error bars correspond to the maximum discrepancy of these four fits from the average. We further checked that different system lengths lead to similar results.

The LL parameters of the ladder system (2) for the BPCB couplings (39) are presented in Fig. 23 as a function of the magnetization per rung. Additionally, we show the parameters of the spin chain mapping [computed for the spin chain Hamiltonian (13)] for comparison. When the ladder is just getting magnetized, or when the ladder is almost fully polarized, $K \to 1$ (free fermion limit) and $u \to 0$ (because of the low density of triplets in the first case, and low density of singlets in the second case). For the spin chain mapping, the reflection symmetry at $m^z = 0.5$ arises from the symmetry under π rotation around the x or y axis of the spin chain. This symmetry has no reason to be present in the original ladder model, and is an artefact of the strong coupling limit, when truncated to the lowest-order term as shown in Appendix A. The values for the spin ladder with the compound BPCB parameters can deviate strongly from this symmetry. The velocity u and the prefactor B_x remain very close to the values for the spin chain mapping. In contrast, the prefactors A_z, A_x, and the exponent K deviate considerably, and A_x and K become strongly asymmetric. The origin of the asymmetry lies in the contribution of the higher triplet states,[2] and can be understood by using a strong coupling expansion of the Hamiltonian (2) up to the second order in γ (see Appendix A4). This asymmetry has consequences for many experimentally relevant quantities, and it was found to cause, for example, strong asymmetries in the 3D order parameter, its transition temperature, and the NMR relaxation rate (see Figs. 10, 9, and 8, respectively).

2. Dynamical LL correlations

In this section we summarize previous results of the LL description of the dynamical correlation functions[19,20,96] at zero temperature. Note that the weak and strong coupling limits, which have been studied separately,[19,20] can be connected.[2] The expression of the correlations in the whole regime is given by[75]

$$S_0^{zz}(q,\omega) = (2\pi m^z)^2\delta(q)\delta(\omega) + \frac{\pi^2 A_z}{u\Gamma(K)^2}\Bigg(\Theta(\omega - u|q-2\pi m^z|)\left[\frac{4u^2}{\omega^2 - u^2(q-2\pi m^z)^2}\right]^{1-K} + \Theta(\omega - u|q - 2\pi(1-m^z)|)\left\{\frac{4u^2}{\omega^2 - u^2[q-2\pi(1-m^z)]^2}\right\}^{1-K}\Bigg) + \frac{K\omega}{u}\Theta(\omega)[\delta(\omega - uq) + \delta(\omega + uq)], \tag{B4}$$

$$S_\pi^{+-}(q,\omega) = \frac{8\pi^2 A_x}{u\Gamma(1/4K)^2}\Theta(\omega - u|q-\pi|)\left[\frac{4u^2}{\omega^2 - u^2(q-\pi)^2}\right]^{1-1/4K} + \frac{4\pi^2 B_x}{u\Gamma(\eta_+)\Gamma(\eta_-)}\Bigg(\Theta(\omega - u|q-\pi(1-2m^z)|)\left\{\frac{2u}{\omega - u[q-\pi(1-2m^z)]}\right\}^{1-\eta_-}\left\{\frac{2u}{\omega + u[q-\pi(1-2m^z)]}\right\}^{1-\eta_+} + \Theta(\omega - u|q-\pi(1+2m^z)|)\left\{\frac{2u}{\omega - u[q-\pi(1+2m^z)]}\right\}^{1-\eta_+}\left\{\frac{2u}{\omega + u[q-\pi(1+2m^z)]}\right\}^{1-\eta_-}\Bigg), \tag{B5}$$

with the Heaviside function $\Theta(x)$ and $\eta_\pm = 1/4K \pm 1 + K$. The correlation S_π^{-+} is obtained by replacing $m^z \to -m^z$ in the S_π^{+-} expression, Eq. (B5).

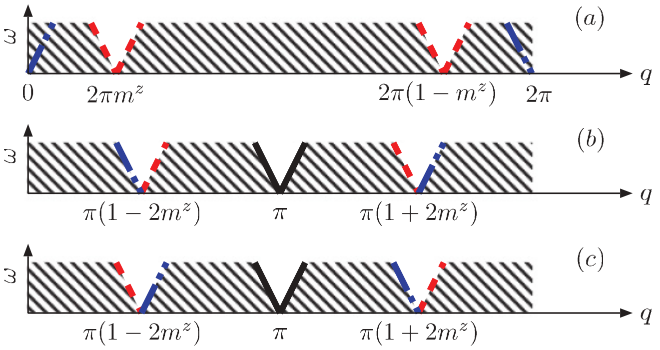

FIG. 24. (Color online) Map of the momentum-frequency low-energy correlations of the LL model, where the white areas represent the continuum of excitations. In the striped areas no excitations are possible. (a) $S_0^{zz}(q,\omega)$: The dashed-dotted lines (blue) are the excitation peaks close to $q = 0,2\pi$ and the dashed lines (red) are the continuum lower boundary with the edge exponent $1-K$ close to $q = 2\pi m^z, 2\pi(1-m^z)$. (b) $S_\pi^{+-}(q,\omega)$, (c) $S_\pi^{-+}(q,\omega)$: The continuum lower boundary close to $q = \pi,\pi(1\pm 2m^z)$ is represented by solid lines (black) (edge exponent $1-1/4K$), dashed lines (red) (edge exponent $1-\eta_- = 2-1/4K-K$), and dashed-dotted lines (blue) (edge exponent $1-\eta_+ = -1/4K-K$).

Equations (B4) and (B5) exhibit the typical behavior of the frequency-momentum LL correlations: A continuum of low-energy excitations exists with a linear dispersion with a slope given by the LL velocity $\pm u$. The spectral weight at the lower boundary of the continuum displays an algebraic singularity with the exponents related to the LL parameter K. A summary of this behavior is sketched in Fig. 24. For the considered system, the longitudinal correlation S_0^{zz} is predicted to diverge with the exponent $1-K$ at its lower edge. As shown in Fig. 25(a1) the exponent of this divergence is very weak < 0.2 for the parameters of BCPB. The transverse correlations $S_\pi^{\pm\mp}$ exhibit a distinct behavior depending on the considered soft mode. Close to $q = \pi$ the weight diverges with an exponent given by $1-1/4K$. This divergence is strong for the considered parameters [$1-1/4K \approx 3/4 \gg 0$ in Fig. 25(a2)]. In contrast, at the soft mode $q = \pi(1-2m^z),\pi(1+2m^z)$, a divergence (cusp) is predicted at the lower edge with the exponent $2-1/4K-K \approx 3/4$ in Fig. 25(a2) [$-1/4K-K \approx -5/4$ in Fig. 25(a3)].

3. Finite-temperature transverse staggered LL correlation

The determination of the relaxation time T_1^{-1} (see Sec. IV C) and of the transition temperature T_c to the 3D-ordered phase (see Sec. IV D 1) requires the staggered transverse retarded correlation function

$$\chi_a^{xx}(x,t) = -i\Theta(t)(-1)^x\langle[\tilde{S}^x(x,t),\tilde{S}^x(0,0)]\rangle, \tag{B6}$$

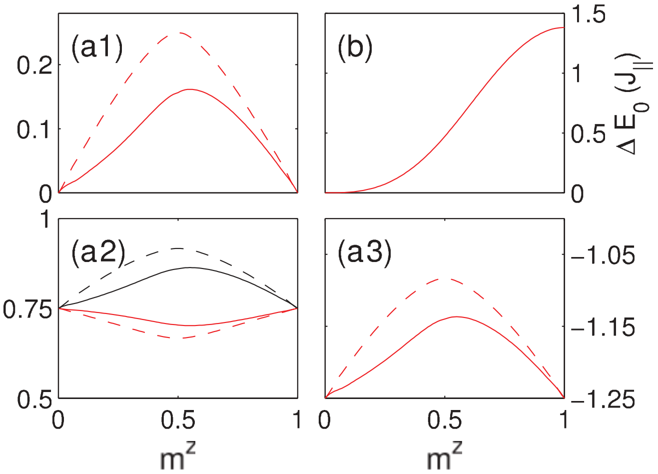

FIG. 25. (Color online) (a) Different exponents that appear in the LL correlation functions, Eqs. (B4) and (B5), vs the magnetization m^z. The solid (dashed) lines are determined from the ladder (spin chain mapping) exponent K in Fig. 23. The exponent $1 - K$ of the S_0^{zz} correlations is shown in (a1), and the exponent $1 - 1/4K$ of the $S_\pi^{\pm\mp}$ correlations at the $q = \pi$ branch is shown in (a2) (lower red curves). The exponents $1 - \eta_- = 2 - 1/4K - K$ (upper black curves) in (a2) and $1 - \eta_+ = -1/4K - K$ in (a3) correspond to both sides of the incommensurate branches of the $S_\pi^{\pm\mp}$ (see Fig. 24). (b) Shift of the ground-state energy per rung vs the magnetization $\Delta E_0(m^z) = E_0(0) - E_0(m^z)$.

written in term of the spin chain mapping operators (12), with $\Theta(t)$ the Heaviside function. In the gapless regime, using the bosonization formalism (17), and taking into account only the most relevant term, we can compute it as described in Ref. 6 for the LL Hamiltonian (16),

$$\chi_a^{xx}(x,t) = -\Theta(t)\Theta(ut-x)\Theta(ut+x)\left(\frac{\pi}{\beta u}\right)^{\frac{1}{2K}} \times \frac{2A_x \sin\left(\frac{\pi}{4K}\right)}{\left|\sinh\left[\frac{\pi}{\beta}\left(\frac{x}{u}+t\right)\right]\sinh\left[\frac{\pi}{\beta}\left(\frac{x}{u}-t\right)\right]\right|^{\frac{1}{4K}}}, \tag{B7}$$

and its Fourier transform,

$$\chi_a^{xx}(q,\omega) = -\frac{A_x \sin\left(\frac{\pi}{4K}\right)}{u}\left(\frac{2\pi}{\beta u}\right)^{\frac{1}{2K}-2} \times B\left[-i\frac{\beta(\omega-uq)}{4\pi}+\frac{1}{8K},1-\frac{1}{4K}\right] \times B\left[-i\frac{\beta(\omega+uq)}{4\pi}+\frac{1}{8K},1-\frac{1}{4K}\right], \tag{B8}$$

where $B(x,y) = \frac{\Gamma(x)\Gamma(y)}{\Gamma(x+y)}$.

APPENDIX C: DMRG METHOD

In this Appendix, we describe first the t-DMRG method and its extension to finite temperature. Then we give the technical details related to the computation of the momentum-frequency correlations.

1. Time-dependent DMRG

The time-dependent DMRG[37–40] (t-DMRG) method is based on the principle of the original DMRG to choose an effective reduced Hilbert space to describe the physics one is interested in. Instead of choosing only once the effective description for the evolution of the state, the t-DMRG adapts its effective description at each time step. The implementation of this idea can be performed using different time-evolution algorithms. Here we use the second-order Trotter-Suzuki expansion for the time-evolution operator by using a rung as a unit.[38,39] The errors arising in this method are the so-called truncation error and the Trotter-Suzuki error. Both are very well controlled (see Ref. 97 for a detailed discussion).

2. Finite-temperature DMRG

The main idea of the finite-temperature DMRG[41–43] (T-DMRG) is to represent the density matrix of the physical state as a pure state in an artificially enlarged Hilbert space. The auxiliary system is constructed by simply doubling the physical system. Starting from the infinite-temperature limit, the finite temperature is reached evolving down in imaginary time. The infinite-temperature state in this auxiliary system corresponds to the totally mixed Bell state $|\psi(0)\rangle = \frac{1}{N_\lambda^{L/2}}\prod_{l=1}^{L}\sum_{\lambda_l}|\lambda_l\lambda_l\rangle$, where $|\lambda_l\lambda_l\rangle$ is the state at the bond l of the auxiliary system that has the same value λ_l on the two sites of the bond (physical and its copy). The sum $\sum_{\lambda_l}$ is done on all these N_λ states $|\lambda_l\rangle$. We evolve the physical part of $|\psi(0)\rangle$ in imaginary time to obtain

$$|\psi(\beta)\rangle = e^{-\beta H/2}|\psi(0)\rangle \tag{C1}$$

by using the t-DMRG algorithm presented in Appendix C1 with imaginary time. We renormalize this state at each step of the imaginary time evolution. Thus the expectation value of an operator O acting in the physical system with respect to the normalized state $|\psi(\beta)\rangle$ is directly related to its thermodynamic average, i.e.,

$$\langle O\rangle_\beta = \frac{\mathrm{Tr}[Oe^{-\beta H}]}{\mathrm{Tr}[e^{-\beta H}]} = \langle\psi(\beta)|O|\psi(\beta)\rangle, \tag{C2}$$

at the temperature $T = 1/\beta$. We use this method to compute the average value of the local rung magnetization $m^z(T)$ and energy per rung $E(T)$ in the center of the system. Additionally, we extract the specific heat $c(T)$ by

$$c(\beta+\delta\beta/2) \approx -\frac{(\beta+\delta\beta/2)^2}{2\delta\beta}(\langle E\rangle_{\beta+\delta\beta} - \langle E\rangle_\beta), \tag{C3}$$

where $\delta\beta$ is the imaginary time step used in the T-DMRG.

To reach very low temperatures $T \to 0$ for the specific heat, we approximate the energy by its expansion in T,

$$E(T) \approx E_0 + \sum_{i=2}^{n}\alpha_i T^i, \tag{C4}$$

up to $n = 4$. The energy at zero temperature E_0 is determined by a standard $T = 0$ DMRG method. Since $E(T)$ has a minimum at $T = 0$, the linear term in the expansion (C4) does not exist. The numbers α_i $(i = 2,3,4)$ are obtained by fitting the expansion on the low T values of the numerically computed $E(T)$.

Typical system lengths used for the finite-temperature calculations are $L = 80$ ($L = 100$ for the spin chain mapping) keeping a few hundred DMRG states and choosing a temperature step of $\delta\beta = 0.02\ \mathrm{K}^{-1}$ ($\delta\beta = 0.01\ \mathrm{K}^{-1}$ for the spin chain mapping).

Let us note that recently a new method has been developed to treat finite temperatures,[98,99] which is very promising to reach even lower temperatures.

3. Momentum-frequency correlation functions

To obtain the desired frequency-momentum spin-spin correlations [$S^{\alpha\beta}_{q_y}(q,\omega)$ in (31)], we first compute the correlations in space and time,

$$S^{\alpha\beta}_{l,k}(t_n) = \langle 0|e^{it_nH} S^{\alpha}_{l+L/2,k} e^{-it_nH} S^{\beta}_{L/2,1}|0\rangle, \tag{C5}$$

with $l = -L/2+1, -L/2+2, \ldots, L/2$, $k = 1, 2$, and $t_n = n\delta t$ ($n = 0,1,\ldots,N_t$) is the discrete time used. These correlations are calculated by time evolving the ground state $|\psi_0\rangle = |0\rangle$ and the excited state $|\psi_1\rangle = S^{\beta}_{L/2,1}|0\rangle$ by using the t-DMRG (see Appendix C 1).

Afterward the overlap of $S^{\alpha}_{l+L/2,k}|\psi_1(t)\rangle$ and $|\psi_0(t)\rangle$ is evaluated to obtain the correlation function (C5).

In an infinite system reflection symmetry would be fulfilled. To minimize the finite system corrections and to recover the reflection symmetry of the correlations, we average them:

$$\tfrac{1}{2}\left[S^{\alpha\beta}_{-l,k}(t_n) + S^{\alpha\beta}_{l,k}(t_n)\right] \rightarrow S^{\alpha\beta}_{l,k}(t_n). \tag{C6}$$

We then compute the symmetric (antisymmetric) correlations (upon leg exchange) (see Sec. V A),

$$S^{\alpha\beta}_{l,q_y}(t_n) = 2\left[S^{\alpha\beta}_{l,1}(t_n) \pm S^{\alpha\beta}_{l,2}(t_n)\right], \tag{C7}$$

with the rung momentum $q_y = 0, \pi$, respectively. Finally, we perform a numerical Fourier transform,[100]

$$S^{\alpha\beta}_{q_y}(q,\omega) \approx \delta t \sum_{n=-N_t+1}^{N_t} \sum_{l=-L/2+1}^{L/2} e^{i(\omega t_n - ql)} S^{\alpha\beta}_{l,q_y}(t_n), \tag{C8}$$

for discrete momenta $q = 2\pi k/L$ ($k = 0,1,\ldots,L-1$) and frequencies ω.[101] The momentum q has the reciprocal units of the interrung spacing a ($a = 1$ is used if not mentioned otherwise). Due to the finite time step δt, our computed $S^{\alpha\beta}_{q_y}(q,\omega)$ are limited to the frequencies from $-\pi/\delta t$ to $\pi/\delta t$. The finite calculation time $t_f = N_t\delta t$ induces artificial oscillations of frequency $2\pi/t_f$ in $S^{\alpha\beta}_{q_y}(q,\omega)$. To eliminate these artefacts and reduce the effects of the finite system length, we apply a filter to the time-space correlations before the numerical Fourier transform (C8), i.e.,

$$S^{\alpha\beta}_{l,q_y}(t_n) f(l,t_n) \rightarrow S^{\alpha\beta}_{l,q_y}(t_n). \tag{C9}$$

We tried different functional forms for the filter $f(l,t_n)$ (cf. Ref. 38 as well). In the following, the results are obtained by a Gaussian filter, $f(l,t_n) = e^{-(4l/L)^2-(2t_n/t_f)^2}$, if not stated otherwise. As the effect of this filtering on the momentum-energy correlations consists to convolve them by a Gaussian function $f(q,\omega) = t_f L/(32\pi) e^{-(\omega t_f/4)^2-(qL/8)^2}$, it minimizes the numerical artefacts but further reduces the momentum-frequency resolution.

Typical values we used in the simulations are system lengths of up to $L = 160$ sites while keeping a few hundreds DMRG states. We limited the final time t_f to be smaller than the time necessary for the excitations to reach the boundaries ($t_f \sim L/2u$ with u the LL velocity in Fig. 23) in order to minimize the boundary effects. The computations for the BPCB parameters, Eq. (39), were typically done with a time step of $\delta t = 0.0355 J_\parallel{}^{-1}$ up to $t_f = 71 J_\parallel{}^{-1}$ (but calculating the correlations only every second time step). The momentum-frequency limitations are then $\delta\omega \approx 0.11 J_\parallel$ and $\delta q \approx 0.1a^{-1}$. Concerning the other couplings and the spin chain calculations, we used a time step $\delta t = 0.1 J_\parallel{}^{-1}$ up to $t_f = 100 J_\parallel{}^{-1}$ (also with the correlation evaluations every second time steps) for a momentum-frequency precision $\delta\omega \approx 0.08 J_\parallel$ and $\delta q \approx 0.1a^{-1}$.

Different techniques of extrapolation in time (by using linear prediction or fitting the long-time evolution with a guess asymptotic form; cf. Refs. 102 and 103) were recently used to improve the frequency resolution of the computed correlations. Nevertheless, as none of them can be apply systematically for our ladder system due to the presence of the high-energy triplet excitations (which result in very-high-frequency oscillations), we decided not to use them.

APPENDIX D: QMC DETERMINATION OF THE 3D-ORDERING TRANSITION T_c

The 3D network of couplings of the coupled ladder Hamiltonian Eq. (1) and shown in Fig. 18 is not frustrated, and can therefore be simulated by using QMC algorithms. We employ a stochastic series expansion implementation with directed loop updates[63] provided with the ALPS libraries.[64,65] This numerical exact approach is complementary to mean-field approaches, because the latter tend not to be quantitatively accurate due to the neglect of quantum fluctuations in the interladder coupling.

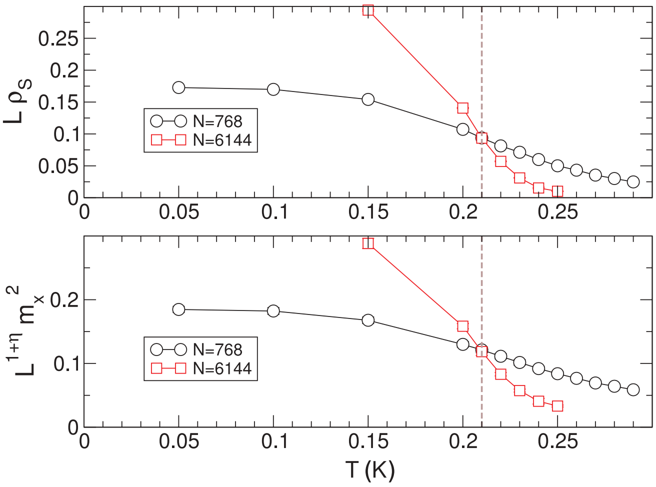

FIG. 26. (Color online) QMC simulation results for the spin stiffness scaling (upper panel), and the order parameter scaling (lower panel). The vertical dashed line denotes the coinciding estimate of T_c from the crossing curves in both panels.

In order to detect the transition temperature we measure the spin stiffness ρ_s based on winding numbers in the three spatial directions. As pointed out in Ref. 104, when plotting $L\rho_s$ for different system sizes L, the different curves cross at T_c. Alternatively, we measured the squared order parameter m_x^2. The quantity $L^{1+\eta}m_x^2$ (assuming the 3D *XY* universality class value of $\eta \approx 0.04$) also crosses at T_c when plotted for different L.

Previously the 3D ordering temperatures of coupled spin ladders in a magnetic field have been determined by using a specific feature of the magnetization $m(T)$.[22] It turns out that while the feature in $m(T)$ indeed locates T_c accurately for simple coupled dimer systems,[105] the same does not hold for coupled ladders. In the ladder case one has to resort to the spin stiffness crossing or order parameter measurements to locate T_c accurately.

When simulating the coupled ladder Hamiltonian, a suitable finite-size sample setup is required. due to the spatial anisotropies in the problem—the ladder direction being singled out over the two transverse spatial directions—an appropriate aspect ratio needs to be kept.[71] In our simulations we chose an aspect ratio of ∼12, i.e., the samples were 12 times longer along the ladder direction than in the transverse directions.

In Fig. 26 we show simulation results for one particular set of couplings: The rung and leg couplings were set to $J_\perp = 12.9$ K and $J_\parallel = 3.3$ K, respectively, the g factor was 2.17, the magnetic field amounted to 8.9 T, and the interladder coupling J' was set to 80 mK. These couplings are identical to those used in Ref. 31. In the upper panel we show the rescaled spin stiffness $L\rho_s$ for two different system sizes (768 spins versus 6144 spins). One locates a crossing at 210 mK for this observable. In the lower panel we show the rescaled squared order parameter $L^{1+\eta}m_x^2$, which also exhibits a crossing at the same temperature. These matching estimates for the critical temperature render us confident that we accurately locate the critical temperature.

Based on this and subsequent simulations either with an identical J' but a higher magnetic field of 11.9 T, or the same field and a smaller $J' = 50$ mK, we are able to determine and verify the use of a single rescaling factor $\alpha = 0.74(1)$ relating the real and effective mean-field interladder coupling,[71] as presented in Sec. IV D 1.

---

[1] A. Auerbach, *Interacting Electrons and Quantum Magnetism*, 2nd ed. (Springer, Berlin, 1998).

[2] T. Giamarchi and A. M. Tsvelik, Phys. Rev. B **59**, 11398 (1999).

[3] T. Nikuni, M. Oshikawa, A. Oosawa, and H. Tanaka, Phys. Rev. Lett. **84**, 5868 (2000).

[4] C. Rüegg, N. Cavadini, A. Furrer, H.-U. Güdel, K. Krämer, H. Mutka, A. Wildes, K. Habicht, and P. Vorderwisch, Nature (London) **423**, 62 (2003).

[5] T. Giamarchi, C. Rüegg, and O. Tchernyshyov, Nat. Phys. **4**, 198 (2008).

[6] T. Giamarchi, *Quantum Physics in One Dimension* (Oxford University Press, Oxford, 2004).

[7] A. O. Gogolin, A. A. Nersesyan, and A. M. Tsvelik, *Bosonization and Strongly Correlated Systems* (Cambridge University Press, Cambridge, UK, 1999).

[8] E. Dagotto and T. M. Rice, Science **271**, 5249 (1996).

[9] S. Gopalan, T. M. Rice, and M. Sigrist, Phys. Rev. B **49**, 8901 (1994).

[10] Zheng Weihong, V. Kotov, and J. Oitmaa, Phys. Rev. B **57**, 11439 (1998).

[11] M. Troyer, H. Tsunetsugu, and D. Würtz, Phys. Rev. B **50**, 13515 (1994).

[12] T. Barnes, E. Dagotto, J. Riera, and E. S. Swanson, Phys. Rev. B **47**, 3196 (1993).

[13] M. Reigrotzki, H. Tsunetsugu, and T. M. Rice, J. Phys. Condens. Matter **6**, 9235 (1994).

[14] W. Zheng, C. J. Hamer, R. R. P. Singh, S. Trebst, and H. Monien, Phys. Rev. B **63**, 144410 (2001).

[15] O. P. Sushkov and V. N. Kotov, Phys. Rev. Lett. **81**, 1941 (1998).

[16] C. Knetter, K. P. Schmidt, M. Grüninger, and G. S. Uhrig, Phys. Rev. Lett. **87**, 167204 (2001).

[17] F. Mila, Eur. Phys. J. B **6**, 201 (1998).

[18] E. Orignac, R. Citro, and T. Giamarchi, Phys. Rev. B **75**, 140403(R) (2007).

[19] R. Chitra and T. Giamarchi, Phys. Rev. B **55**, 5816 (1997).

[20] A. Furusaki and S. C. Zhang, Phys. Rev. B **60**, 1175 (1999).

[21] X. Wang and L. Yu, Phys. Rev. Lett. **84**, 5399 (2000).

[22] S. Wessel, M. Olshanii, and S. Haas, Phys. Rev. Lett. **87**, 206407 (2001).

[23] B. Normand and C. Rüegg, e-print arXiv:1006.4196 (2010).

[24] Y. Maeda, C. Hotta, and M. Oshikawa, Phys. Rev. Lett. **99**, 057205 (2007).

[25] M. Usami and S.-i. Suga, Phys. Rev. B **58**, 14401 (1998).

[26] T. Hikihara and A. Furusaki, Phys. Rev. B **63**, 134438 (2001).

[27] M. Tachiki, T. Yamada, and S. Maekawa, J. Phys. Soc. Jpn. **29**, 663 (1970).

[28] B. R. Patyal, B. L. Scott, and R. D. Willett, Phys. Rev. B **41**, 1657 (1990).

[29] C. Rüegg, K. Kiefer, B. Thielemann, D. F. McMorrow, V. Zapf, B. Normand, M. B. Zvonarev, P. Bouillot, C. Kollath, T. Giamarchi, S. Capponi, D. Poilblanc, D. Biner, and K. W. Krämer, Phys. Rev. Lett. **101**, 247202 (2008).

[30] M. Klanjšek, H. Mayaffre, C. Berthier, M. Horvatić, B. Chiari, O. Piovesana, P. Bouillot, C. Kollath, E. Orignac, R. Citro, and T. Giamarchi, Phys. Rev. Lett. **101**, 137207 (2008).

[31] B. Thielemann, C. Rüegg, K. Kiefer, H. M. Rønnow, B. Normand, P. Bouillot, C. Kollath, E. Orignac, R. Citro, T. Giamarchi, A. M. Läuchli, D. Biner, K. W. Krämer, F. Wolff-Fabris, V. S. Zapf, M. Jaime, J. Stahn, N. B. Christensen, B. Grenier, D. F. McMorrow, and J. Mesot, Phys. Rev. B **79**, 020408(R) (2009).

[32] B. Thielemann, C. Rüegg, H. M. Rønnow, A. M. Läuchli, J.-S. Caux, B. Normand, D. Biner, K. W. Krämer, H.-U. Güdel, J. Stahn, K. Habicht, K. Kiefer, M. Boehm, D. F. McMorrow, and J. Mesot, Phys. Rev. Lett. **102**, 107204 (2009).

[33] A. T. Savici, G. E. Granroth, C. L. Broholm, D. M. Pajerowski, C. M. Brown, D. R. Talham, M. W. Meisel, K. P. Schmidt, G. S. Uhrig, and S. E. Nagler, Phys. Rev. B **80**, 094411 (2009).

[34] I. Bloch, J. Dalibard, and W. Zwerger, Rev. Mod. Phys. **80**, 885 (2008).

[35] J.-S. Caux, R. Hagemans, and J.-M. Maillet, J. Stat. Mech.: Theor. Exp. (2005) P09003.

[36] J.-S. Caux, P. Calabrese, and N. A. Slavnov, J. Stat. Mech.: Theory Exp. (2007) P01008.

[37] G. Vidal, Phys. Rev. Lett. **93**, 040502 (2004).

[38] S. R. White and A. E. Feiguin, Phys. Rev. Lett. **93**, 076401 (2004).

[39] A. Daley, C. Kollath, U. Schollwöck, and G. Vidal, J. Stat. Mech.: Theory Exp. (2004) P04005.

[40] U. Schollwöck and S. R. White, in *Effective Models for Low-Dimensional Strongly Correlated Systems*, edited by G. G. Batrouni and D. Poilblanc (AIP, Melville, NY, 2006), p. 155.

[41] F. Verstraete, J. J. García-Ripoll, and J. I. Cirac, Phys. Rev. Lett. **93**, 207204 (2004).

[42] M. Zwolak and G. Vidal, Phys. Rev. Lett. **93**, 207205 (2004).

[43] A. E. Feiguin and S. R. White, Phys. Rev. B **72**, 220401 (2005).

[44] H. J. Schulz, Phys. Rev. B **34**, 6372 (1986).

[45] I. Affleck, Phys. Rev. B **41**, 6697 (1990).

[46] S. Sachdev, T. Senthil, and R. Shankar, Phys. Rev. B **50**, 258 (1994).

[47] M. Tachiki and T. Yamada, J. Phys. Soc. Jpn. **28**, 1413 (1970).

[48] G. Chaboussant, M.-H. Julien, Y. Fagot-Revurat, M. Hanson, L. Lévy, C. Berthier, M. Horvatic, and O. Piovesana, Eur. Phys. J. B **6**, 167 (1998).

[49] S. R. White, Phys. Rev. B **48**, 10345 (1993).

[50] U. Schollwöck, Rev. Mod. Phys. **77** (2005).

[51] K. A. Hallberg, Adv. Phys. **55**, 477 (2006).

[52] E. Jeckelmann, Prog. Theor. Phys. Suppl. **176**, 143 (2008).

[53] M. Gaudin, *La fonction d'onde de Bethe* (Masson, Paris, 1983).

[54] V. E. Korepin, N. M. Bogoliubov, and A. G. Izergin, *Quantum Inverse Scattering Method and Correlation Functions* (Cambridge University Press, Cambridge, UK, 1993).

[55] M. Takahashi and M. Suzuki, Prog. Theor. Phys. **48**, 2187 (1972).

[56] M. Takahashi, Prog. Theor. Phys. **51**, 1348 (1974).

[57] M. Takahashi, Phys. Rev. B **44**, 12382 (1991).

[58] H. J. Schulz, Phys. Rev. Lett. **77**, 2790 (1996).

[59] N. Nagaosa, Phys. Rev. B **39**, 2188 (1989).

[60] S. Coleman, Phys. Rev. D **11**, 2088 (1975).

[61] A. Luther, Phys. Rev. B **14**, 2153 (1976).

[62] S. Lukyanov and A. B. Zamolodchikov, Nucl. Phys. B **493**, 571 (1997).

[63] O. F. Syljuåsen and A. W. Sandvik, Phys. Rev. E **66**, 046701 (2002).

[64] F. Alet, S. Wessel, and M. Troyer, Phys. Rev. E **71**, 036706 (2005).

[65] A. Albuquerque, F. Alet, P. Corboz, P. Dayal, A. Feiguin, S. Fuchs, L. Gamper, E. Gull, S. Gürtler, A. Honecker, R. Igarashi, M. Körner, A. Kozhevnikov, A. Läuchli, S. Manmana, M. Matsumoto, I. McCulloch, F. Michel, R. Noack, G. Pawlowski, L. Pollet, T. Pruschke, U. Schollwöck, S. Todo, S. Trebst, M. Troyer, P. Werner, and S. Wessel, J. Magn. Magn. Mater. **310**, 1187 (2007).

[66] The perturbative expression of the ground state in the spin liquid regime and the corresponding singlet and triplet densities are given in Appendix A.

[67] An additional scaling factor 7.47 mJ/gK has to be applied on the theoretical specific heat (per rung) to convert to the experimental units.

[68] S. Suga, J. Phys. Soc. Jpn. **77**, 074717 (2008).

[69] C. P. Slichter, *Principles of Magnetic Resonance* (Springer, Berlin, 1980).

[70] D. J. Scalapino, Y. Imry, and P. Pincus, Phys. Rev. B **11**, 2042 (1975).

[71] C. Yasuda, S. Todo, K. Hukushima, F. Alet, M. Keller, M. Troyer, and H. Takayama, Phys. Rev. Lett. **94**, 217201 (2005).

[72] S. Todo and A. Shibasaki, Phys. Rev. B **78**, 224411 (2008).

[73] G. Müller, H. Thomas, H. Beck, and J. C. Bonner, Phys. Rev. B **24**, 1429 (1981).

[74] A. M. Läuchli, Manep Meeting, Les Diablerets (2007).

[75] Note that the edge exponents in the incommensurate branches of the correlations (B5) are inverted compared to their expression in Ref. 20.

[76] S. Sorella and A. Parola, Phys. Rev. Lett. **76**, 4604 (1996).

[77] S. Sorella and A. Parola, Phys. Rev. B **57**, 6444 (1998).

[78] For the correlations S_π^{zz} and S_0^{+-}, some of these singularities correspond to the lower edge description in Ref. 20 and discussed in Sec. V C 3 a.

[79] A. M. Läuchli and C. Rüegg (unpublished).

[80] A. K. Kolezhuk and H.-J. Mikeska, Phys. Rev. B **65**, 014413 (2001).

[81] A. K. Kolezhuk and H.-J. Mikeska, Prog. Theor. Phys. Suppl. **145**, 85 (2002).

[82] A. Friedrich, A. K. Kolezhuk, I. P. McCulloch, and U. Schollwöck, Phys. Rev. B **75**, 094414 (2007).

[83] Note that in the strong coupling limit the energy scales set by $J_\perp$ and h^z become very close, such that this position is in agreement with the ones previously discussed for the strong coupling limit.

[84] B. C. Watson, V. N. Kotov, M. W. Meisel, D. W. Hall, G. E. Granroth, W. T. Montfrooij, S. E. Nagler, D. A. Jensen, R. Backov, M. A. Petruska, G. E. Fanucci, and D. R. Talham, Phys. Rev. Lett. **86**, 5168 (2001).

[85] F. Anfuso, M. Garst, A. Rosch, O. Heyer, T. Lorenz, C. Rüegg, and K. Krämer, Phys. Rev. B **77**, 235113 (2008).

[86] T. Lorenz, O. Heyer, M. Garst, F. Anfuso, A. Rosch, C. Rüegg, and K. Krämer, Phys. Rev. Lett. **100**, 067208 (2008).

[87] E. Čižmár, M. Ozerov, J. Wosnitza, B. Thielemann, K. W. Krämer, C. Rüegg, O. Piovesana, M. Klanjšek, M. Horvatić, C. Berthier, and S. A. Zvyagin, Phys. Rev. B **82**, 054431 (2010).

[88] These parameters were the first outputs from the NMR measurements, which were later refined to the values from Ref. 30. Note that small changes in these values do not affect the main results of the calculations.

[89] S. W. Lovesey, *Theory of Neutron Scattering from Condensed Matter* (Oxford University Press, New York, 1986).

[90] C. Rüegg, B. Normand, M. Matsumoto, C. Niedermayer, A. Furrer, K. W. Krämer, H.-U. Güdel, P. Bourges, Y. Sidis, and H. Mutka, Phys. Rev. Lett. **95**, 267201 (2005).

[91] S. Sachdev and R. N. Bhatt, Phys. Rev. B **41**, 9323 (1990).

[92] J.-D. Picon, A. F. Albuquerque, K. P. Schmidt, N. Laflorencie, M. Troyer, and F. Mila, Phys. Rev. B **78**, 184418 (2008).

[93] T. Hikihara and A. Furusaki, Phys. Rev. B **69**, 064427 (2004).

[94] M. Klanjšek, H. Mayaffre, C. Berthier, M. Horvatić, B. Chiari, O. Piovesana, P. Bouillot, C. Kollath, E. Orignac, R. Citro, and T. Giamarchi, Phys. Status Solidi B **247**, 656 (2010).

[95] F. D. M. Haldane, Phys. Rev. Lett. **45**, 1358 (1980).

[96] M. Sato, T. Momoi, and A. Furusaki, Phys. Rev. B **79**, 060406 (2009).

[97] D. Gobert, C. Kollath, U. Schollwöck, and G. Schütz, Phys. Rev. E **71**, 036102 (2005).

[98] S. R. White, Phys. Rev. Lett. **102**, 190601 (2009).

[99] E. Stoudenmire and S. R. White, New J. Phys. **12**, 055026 (2010).

[100] In order to delete the numerical artefacts appearing in the zero-frequency component of $S^{zz}_0(q,\omega)$ due to the boundary effects and the limitation in the numerical precision, we compute the Fourier transform of $S^{zz}_{l,0}(t_n)$ only with its imaginary part that has no zero-frequency component as proposed in Ref. 106.

[101] The negative time correlations in the sum for $n < 0$ are deduced from their value at positive time because $S^{\alpha\beta}_{q_y}(q,-t_n) = S^{\alpha\beta\dagger}_{q_y}(q,t_n)$, with $S^{\alpha\beta}_{q_y}(q,t_n) = \sum_l e^{-iql} S^{\alpha\beta}_{l,q_y}(t_n)$, for translation-invariant systems, and for correlations such as $S^{\alpha\dagger} = S^{\beta}$ with $\alpha,\beta = z,+,-$.

[102] S. R. White and I. Affleck, Phys. Rev. B **77**, 134437 (2008).

[103] T. Barthel, U. Schollwöck, and S. R. White, Phys. Rev. B **79**, 245101 (2009).

[104] A. W. Sandvik, Phys. Rev. Lett. **80**, 5196 (1998).

[105] O. Nohadani, S. Wessel, B. Normand, and S. Haas, Phys. Rev. B **69**, 220402 (2004).

[106] R. G. Pereira, S. R. White, and I. Affleck, Phys. Rev. B **79**, 165113 (2009).